JAMES | Journal of Advances in Modeling Earth Systems

RESEARCH ARTICLE
10.1029/2022MS003192

Key Points:

- The CESM2.2 release includes several enhancements to the spectral-element dynamical core, including two Arctic refined mesh configurations
- Quasi-uniform unstructured grids degrade Greenland mass balance compared to latitude-longitude grids at the conventional 1° resolution
- The refined Arctic meshes substantially improve the surface mass balance over conventional grid resolutions

Correspondence to:
A. R. Herrington,
aherring@ucar.edu

Citation:
Herrington, A. R., Lauritzen, P. H., Lofverstrom, M., Lipscomb, W. H., Gettelman, A., & Taylor, M. A. (2022). Impact of grids and dynamical cores in CESM2.2 on the surface mass balance of the Greenland Ice Sheet. *Journal of Advances in Modeling Earth Systems*, *14*, e2022MS003192. https://doi.org/10.1029/2022MS003192

Received 23 MAY 2022
Accepted 27 SEP 2022

Impact of Grids and Dynamical Cores in CESM2.2 on the Surface Mass Balance of the Greenland Ice Sheet

Adam R. Herrington[1], Peter H. Lauritzen[1], Marcus Lofverstrom[2], William H. Lipscomb[1], Andrew Gettelman[1], and Mark A. Taylor[3]

[1]National Center for Atmospheric Research, Boulder, CO, USA, [2]Department of Geosciences, University of Arizona, Tucson, AZ, USA, [3]Sandia National Laboratories, Albuquerque, NM, USA

Abstract Six different configurations, a mixture of grids and atmospheric dynamical cores available in the Community Earth System Model, version 2.2 (CESM2.2), are evaluated for their skill in representing the climate of the Arctic and the surface mass balance of the Greenland Ice Sheet (GrIS). The finite-volume dynamical core uses structured, latitude-longitude grids, whereas the spectral-element dynamical core is built on unstructured meshes, permitting grid flexibility such as quasi-uniform grid spacing globally. The 1°–2° latitude-longitude and quasi-uniform unstructured grids systematically overestimate both accumulation and ablation over the GrIS. Of these 1°–2° grids, the latitude-longitude grids outperform the quasi-uniform unstructured grids because they have more degrees of freedom to represent the GrIS. Two Arctic-refined meshes, with 1/4° and 1/8° refinement over Greenland, were developed for the spectral-element dynamical core and are documented here as newly supported configurations in CESM2.2. The Arctic meshes substantially improve the simulated clouds and precipitation rates in the Arctic. Over Greenland, these meshes skillfully represent accumulation and ablation processes, leading to a more realistic GrIS surface mass balance. As CESM is in the process of transitioning away from conventional latitude-longitude grids, these new Arctic-refined meshes improve the representation of polar processes in CESM by recovering resolution lost in the transition to quasi-uniform grids, albeit at increased computational cost.

Plain Language Summary The mass balance of Earth's big ice sheets is crucially important for understanding controls on global sea-level rise. However, the scale of the processes needed to represent ice sheet mass balance is challenging to resolve in conventional Earth System Models. This study evaluates the ability of different grids and atmospheric solvers (i.e., the dynamical core) in CESM2.2 to resolve the surface mass balance (SMB) of the Greenland Ice Sheet. We show that the ongoing transition away from latitude-longitude grids, toward quasi-uniform unstructured grids in CESM2.2 leads to a degradation of the simulated SMB. Two variable-resolution grids with enhanced resolution over Greenland are developed and incorporated into the release of CESM2.2, which substantially improves the SMB over the latitude longitude grids.

1. Introduction

General Circulation Models (GCMs) are powerful tools for understanding the meteorology and climate of the high latitudes, which are among the most sensitive regions on Earth to global and environmental change. GCMs differ vastly in their numerical treatment of polar regions because of the so-called *pole problem* (Williamson, 2007). The pole problem refers to numerical instability arising from the convergence of meridian lines into polar singularities on latitude-longitude grids (e.g., Figure 1a, hereafter referred to as *lat-lon* grids). Depending on the numerics, methods exist to suppress this instability, and lat-lon grids may be advantageous for polar processes by representing structures with finer resolution than elsewhere in the computational domain. With the recent trend toward quasi-uniform unstructured grids, any potential benefits of lat-lon grids in polar regions may be lost (hereafter, *quasi-uniform* refers to approximately isotropic grids, in contrast to lat-lon grids, which are highly anisotropic due to the polar singularity). In this study, we evaluate a number of grids and dynamical cores (hereafter referred to as *dycores*) available in the Community Earth System Model, version 2.2 (CESM2.2; Danabasoglu et al., 2020), including new variable-resolution grids (i.e., grids with enhanced resolution over a particular region), to understand their impacts on the simulated Arctic climate. We focus specifically on the climate and surface mass balance of the Greenland Ice Sheet.

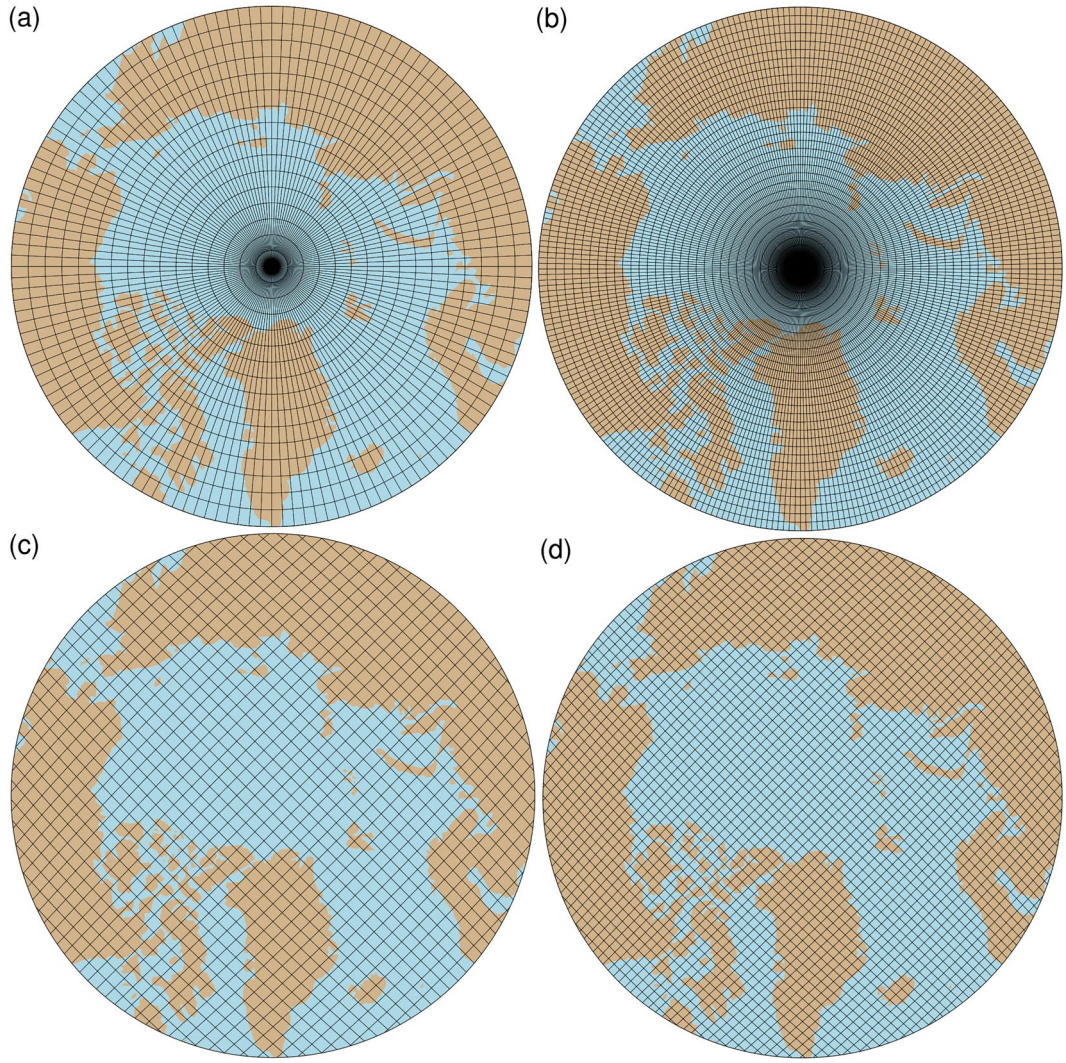

Figure 1. Computational grids for the 1°–2° lat-lon and quasi-uniform unstructured grids in this study, using a northern hemisphere polar projection. Grids names after Table 1, (a) 2° lat-lon grid (`f19`), (b) 1° lat-lon grid (`f09`), (c) 1° quasi-uniform unstructured grid with reduced physics resolution (`ne30pg2`) and (d) 1° quasi-uniform unstructured grid (`ne30pg3`).

In the 1970s, the pole problem was largely defeated through the adoption of efficient spectral transform methods in GCMs (see Williamson, 2007, and references therein). These methods transform grid point fields into a global, isotropic representation in wave space, where linear operators (e.g., horizontal derivatives) in the (truncated) equation set can be solved exactly. While spectral transform methods are still used today, local numerical methods have become desirable for their ability to run efficiently on massively parallel systems. The pole problem has thus re-emerged in contemporary climate models that use lat-lon grids, and some combination of reduced grids (modified lat-lon grids in which cells around the polar singularity are elongated in the zonal direction) and polar filters are necessary to ameliorate this numerical instability (Jablonowski & Williamson, 2011). Polar filters subdue the growth of unstable computational modes by applying additional damping to the numerical solution over polar regions. This damping reduces the effective resolution in polar regions such that the resolved scales are *approximately* the same everywhere on the grid. We emphasize *approximately*, since it is conceivable that marginal increases in effective resolution occur over polar regions in lat-lon grids, despite polar filtering, since resolved waves can be represented with more grid points than at lower latitudes.

Dycores built on lat-lon grids have some advantages over dycores built on unstructured grids. Lat-lon coordinate lines are orthogonal, and aligned with zonally symmetric circulations that characterize many large-scale features

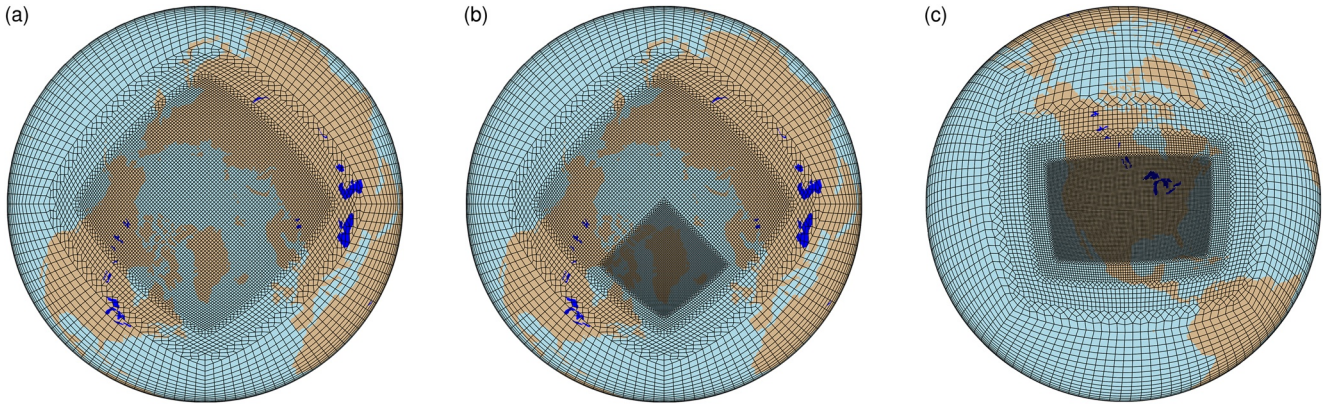

Figure 2. Variable-resolution grids available in CESM2.2, (a) `Arctic`, (b) `Arctic` − GrIS and (c) `CONUS`. Note what is shown is the element grid; the computational grid has 3 × 3 independent grid points per element.

of Earth's atmosphere. Lauritzen et al. (2010) has experimented with rotating lat-lon models such that their coordinate lines no longer align with an idealized, zonally balanced circulation. For the finite-volume lat-lon dycore considered in this paper (hereafter *FV*), numerical errors were shown to be largest when the polar singularity is rotated into the baroclinic zone (45°N latitude), generating spurious wave growth much earlier in the simulation than for other rotation angles. This illustrates the advantages of coordinate surfaces aligned with latitude bands, albeit an extreme example where the polar singularity and the polar filter are also contributing to the spurious wave growth. The unstructured grids all generate spurious baroclinic waves earlier in the simulations than the (unrotated) lat-lon models, although the unstructured model considered in this paper, the spectral-element dycore (hereafter *SE*), holds a balanced zonal flow without spurious wave growth appreciably longer than the rotated FV experiments (Lauritzen et al., 2010). And unlike FV, the SE dycore has the same error characteristics regardless of how the grid is rotated.

The polar filter in the FV model impedes efficiency at large processor (CPU) counts because it requires a spectral transform, which has a large communication overhead (Dennis et al., 2012; Suarez & Takacs, 1995). Unstructured grids support quasi-uniform grid spacing globally, and there is no pole problem (e.g., Figure 1c). This is in part why unstructured grids are becoming more common; their improved performance on massively parallel systems and lack of constraints on grid structure (Putman & Lin, 2007; Taylor et al., 1997; Wan et al., 2013). This increased grid flexibility allows for the adoption of variable-resolution grids (e.g., Figure 2; hereafter abbreviated as *VR*), sometimes referred to as regional grid refinement. In principle, grid refinement over polar regions can make up for any loss of resolution in transitioning away from lat-lon grids (e.g., Figure 2). However, local grid refinement comes at the cost of a smaller CFL-limited time step in the refined region; the CFL-condition—short for Courant–Friedrichs–Lewy condition—is a necessary condition for numerical stability when using discrete data in time and space.

We emphasize that the pole problem is a distinctive feature of the dycore in atmospheric models. Polar filters do not directly interfere with the physical parameterizations, nor do they have any bearing on the surface models; for example, the land model can take full advantage of the greater number of grid cells in polar regions on lat-lon grids. This is particularly relevant for the surface mass balance (*SMB*; the integrated sum of precipitation and runoff) of the Greenland Ice Sheet, which relies on hydrological processes represented in the land model.

The SMB of the Greenland Ice Sheet (hereafter *GrIS*) is determined by processes occurring over a range of scales (Fyke et al., 2018) that are difficult to represent in GCMs (Pollard, 2010). GrIS precipitation is concentrated at the ice-sheet margins, where steep topographic slopes drive orographic precipitation. The truncated topography used by low resolution GCMs enables moisture to penetrate well into the GrIS interior, manifesting as a positive precipitation bias in the interior (Pollard & Groups, 2000; Van Kampenhout et al., 2019). GrIS ablation areas (marginal regions where the annual SMB is negative) are typically less than 100 km wide and are confined to low-lying areas or regions with low precipitation. These narrow ablation zones are not fully resolved in low-resolution GCMs, and may further degrade the simulated SMB. More recently, GCMs such as CESM and the NASA Goddard Institute for Space Studies GCM (Alexander et al., 2019), have implemented an elevation

class downscaling scheme for computing the SMB. The downscaling helps to resolve these narrow ablation zones in GCMs (Sellevold et al., 2019), but large SMB biases remain. For example, CESM, version 2.0 (CESM2) underestimates ablation in the northern GrIS, leading to unrealistic ice advance when run with an interactive ice sheet component (Lofverstrom et al., 2020).

Regional climate models (RCMs) are commonly relied upon to provide more accurate SMB estimates. The limited area domain used by RCMs permits the use of high-resolution grids capable of resolving SMB processes, and can skillfully simulate the GrIS SMB (Box et al., 2004; Fettweis et al., 2013; Mottram et al., 2017; Noël et al., 2018; Rae et al., 2012; Van Angelen et al., 2012). However, unlike GCMs, RCMs are not a freely evolving system, and the atmospheric state must be prescribed at the lateral boundaries of the model domain. The inability of the RCM solution to influence larger-scale dynamics outside the RCM domain (due to the prescribed boundary conditions) severely limits this approach from properly representing the role of the GrIS in the climate system. In addition, the boundary conditions are derived from a separate host model, which introduces inconsistencies due to differences in model design between the host model and the RCM.

In order to retain the benefits of RCMs in a GCM, Van Kampenhout et al. (2019) used the VR capabilities of the SE dycore in CESM, generating grids where Greenland is represented with up to 1/4° resolution, and elsewhere with the more conventional 1° resolution. The simulated SMB compared favorably to the SMB from RCMs and observations. The VR approach is therefore emerging as a powerful tool for simulating and understanding the GrIS and its response to different forcing scenarios.

The SE dycore has been included in the model since CESM version 1, but has been under active development ever since. This includes the switch to a dry-mass vertical coordinate (Lauritzen et al., 2018) and incorporation of an accelerated multi-tracer transport scheme (Lauritzen et al., 2017), made available in CESM2. This paper documents several additional enhancements to the SE dycore as part of the release of CESM2.2. These include three new VR configurations (Figure 2), two Arctic meshes and a Contiguous United-States mesh (CONUS; featured in Pfister et al. [2020]). While there are dozens of published studies using VR in CESM (e.g., Bambach et al., 2021; Burakowski et al., 2019; Gettelman et al., 2017; Rhoades et al., 2016; Zarzycki et al., 2014), these studies either used development code or collaborated closely with model developers. CESM2.2 is the first code release that contains out-of-the-box VR functionality.

This study compares the representation of Arctic regions using the SE and FV dycores in CESM2.2 (see description below), as these two dycores treat high latitudes (i.e., the pole problem) in different ways. Section 2 documents the grids, dycores, and physical parameterizations used in this study, and also describes the experiments, data sets, and evaluation methods. Section 3 analyzes the results of the experiments, and Section 4 provides a general discussion and conclusions.

2. Methods

CESM2.2 is a CMIP6-class (Coupled Model Intercomparison Project Phase 6; Eyring et al., 2016) Earth System Model maintained by the National Center for Atmosphere Research. CESM2.2 contains sub-component models for the atmosphere, land, ocean, sea-ice, and land-ice, and can be configured to run with varying degrees of complexity. All simulations described in this study use an identical transient 1979–1998 Atmospheric Model Intercomparison Project (AMIP) configuration, with prescribed monthly sea-surface temperature and sea ice following Hurrell et al. (2008). In CESM terminology, AMIP simulations use the FHIST computational set and run out of the box in CESM2.2. The land-ice component is not dynamically active in FHIST. However, the surface mass balance is computed by the land model before being passed to the land-ice component; FHIST includes the necessary functionality to simulate the SMB of the Greenland Ice Sheet.

2.1. Dynamical Cores

The atmospheric component of CESM2.2 (Danabasoglu et al., 2020), the Community Atmosphere Model, version 6.3 (CAM6; Craig et al., 2021; Gettelman et al., 2019), supports several different atmospheric dynamical cores. These include dycores on lat-lon grids, such as finite-volume (FV; Lin, 2004) and Eulerian spectral transform (EUL; Collins et al., 2006) models, and dycores built on unstructured grids, including spectral-element (SE; Lauritzen et al., 2018) and finite-volume 3 (FV3; Putman & Lin, 2007) models. This study compares the

performance of the SE and FV dycores, omitting the EUL and FV3 dycores. CESM2 runs submitted to CMIP6 used the FV dycore, whereas the SE dycore is often used for global high-resolution simulations (e.g., Bacmeister et al., 2016; Chang et al., 2020; Small et al., 2014) due to its higher throughput on massively parallel systems (Dennis et al., 2012).

2.1.1. Finite-Volume (FV) Dynamical Core

The FV dycore integrates the hydrostatic equations of motion using a finite-volume discretization on a spherical lat-lon grid (Lin & Rood, 1997). The 2D dynamics evolve in floating Lagrangian layers that are periodically mapped to an Eulerian reference grid in the vertical (Lin, 2004). Hyperviscous damping is applied to the divergent modes, and is increased in the top few layers (referred to as a *sponge layer*) to prevent undesirable interactions with the model top, such as wave reflection (Lauritzen et al., 2011). A polar filter damps computational instability due to the convergence of meridians, permitting a longer time step. It takes the form of a Fourier filter in the zonal direction, with the damping coefficients increasing monotonically in the meridional direction (Suarez & Takacs, 1995). The form of the filter is designed to slow down the propagation of large zonal wave-numbers to satisfy the CFL condition of the shortest resolved wave at some reference latitude.

2.1.2. Spectral-Element (SE) Dynamical Core

The SE dycore integrates the hydrostatic equations of motion using a high-order continuous Galerkin method (Taylor & Fournier, 2010; Taylor et al., 1997). The computational domain is a cubed-sphere grid (obtained by projecting each face of a cube onto a sphere) tiled with quadrilateral elements (see Figure 2). Each element contains a fourth-order basis set in each horizontal direction, with the solution defined at the roots of the basis functions, the Gauss-Lobatto-Legendre quadrature points. This results in 16 nodal points per element, with 12 of the points lying on the (shared) element boundary. Communication between elements uses the direct stiffness summation (Canuto et al., 2007), which applies a numerical flux to the element boundaries to reconcile overlapping nodal values and produce a continuous global basis set.

As with the FV dycore, the dynamics evolve in floating Lagrangian layers that are subsequently mapped to an Eulerian reference grid. A dry mass vertical coordinate was recently implemented for thermodynamic consistency with condensates (Lauritzen et al., 2018). The 2D dynamics have no implicit dissipation, and so hyperviscosity operators are applied to all prognostic variables to remove spurious numerical errors (Dennis et al., 2012). Laplacian damping is applied in the sponge layer.

SE is a next-generation dycore, and is less mature than the FV dycore due to its shorter history. In CESM2.2, the SE numerics have been enhanced relative to CESM2.0 to mitigate spurious noise over topography. These algorithmic changes are described in Appendix A. Future versions of CESM will likely include further optimizations and enhancements to the (more junior) SE dycore.

The SE dycore supports regional grid refinement via its VR configuration, requiring two enhancements over quasi-uniform resolution grids. First, as the numerical viscosity increases with resolution, explicit hyperviscosity relaxes according to the local element size, reducing in strength by an order of magnitude per halving of the grid spacing. A tensor-hyperviscosity formulation is used (Guba et al., 2014), which adjusts the coefficients in two orthogonal directions to more accurately target highly distorted quadrilateral elements. Second, the topography boundary conditions are smoothed in a way that does not excite grid scale modes, and so the NCAR topography software (Lauritzen et al., 2015) has been modified to scale the smoothing radius by the local element size, resulting in rougher topography in the refinement zone.

When using the SE dycore with quasi-uniform grid spacing, the SE tracer transport scheme is replaced with the Conservative Semi-Lagrangian Multi-tracer transport scheme (CSLAM) (Lauritzen et al., 2017). Atmospheric tracers have large, nearly discontinuous horizontal gradients that are difficult to represent with spectral methods, which are prone to oscillatory "Gibbs-ringing" errors (Rasch & Williamson, 1990). CSLAM has improved tracer property preservation and accelerated multi-tracer transport. It uses a separate grid from the spectral-element dynamics, dividing each element into 3×3 control volumes with quasi-equal area. The physical parameterizations are computed from the state on the CSLAM grid, which has clear advantages over the original SE dycore in which the physics are evaluated at Gauss-Lobatto-Legendre points (Herrington et al., 2018). CSLAM advection is not available in the VR configuration, which instead uses the standard SE tracer transport scheme with the physics evaluated at Gauss-Lobatto-Legendre points.

Table 1
Grids and Dycores Used in This Study

grid name	Dycore	Δx_{eq} (km)	Δx_{fine} (km)	Δt_{phys} (s)	Cost (25 nodes)	Cost (50 nodes)
f19	FV	278	-	1,800	436.66	-
f09	FV	139	-	1,800	1534.57	2024.24
ne30pg2	SE-CSLAM	167	-	1,800	1497.26	1683.97
ne30pg3	SE-CSLAM	111	-	1,800	1890.48	2090.43
ne30pg3*	SE-CSLAM	111	-	450	-	-
Arctic	SE	111	28	450	15947.41	16675.45
Arctic − GrIS	SE	111	14	225	40305.03	41036.67

Note. Δx_{eq} is the average equatorial grid spacing, Δx_{fine} is the grid spacing in the refined region (if applicable), and Δt_{phys} is the physics time step. FV refers to the finite-volume dycore, SE the spectral-element dycore, and SE-CSLAM the spectral-element dycore with CSLAM tracer advection. The FV dycore uses lat-lon grids, whereas the SE and SE-CSLAM dycores run on unstructured grids. We use the ne30pg3 grid for two runs with different values of Δt_{phys}. The last columns provide the computational costs in core hours per simulated year (CHPSY). The costs are from single-month runs using 25 nodes and 50 nodes on the Cheyenne supercomputer (Computational and Information Systems Laboratory, 2017).

2.2. Physical Parameterizations

All simulations in this study use the CAM6 physical parameterization package (hereafter referred to as the *physics*; Gettelman et al., 2019). The physics in CAM6 differs from its predecessors through the incorporation of high-order turbulence closure, Cloud Layers Unified by Binormals (CLUBB; Bogenschutz et al., 2013; Golaz et al., 2002), which jointly acts as a planetary boundary layer, shallow convection, and cloud macrophysics scheme. CLUBB is coupled with the MG2 microphysics scheme (Gettelman & Morrison, 2015; Gettelman et al., 2015), which computes prognostic precipitation and uses classical nucleation theory to represent cloud ice for improved cloud-aerosol interactions. Deep convection is parameterized using a convective quasi-equilibrium mass flux scheme (Neale et al., 2008; Zhang & McFarlane, 1995) and includes convective momentum transport (Richter et al., 2010). Boundary layer form drag is modeled after Beljaars et al. (2004), and orographic gravity wave drag is represented with an anisotropic method informed by the orientation of topographic ridges at the sub-grid scale (the ridge orientation is derived from a high-resolution, global topography data set [Danielson & Gesch, 2011]).

Initial simulations with the SE dycore produced weaker shortwave cloud forcing relative to the tuned finite-volume dycore in the standard CESM2 configuration. The SE dycore in CESM2.2 therefore has two CLUBB parameter changes to provide more realistic cloud forcing and top-of-atmosphere radiation balance. We reduced the width of the sub-grid distribution of vertical velocity (clubb_gamma = 0.308 → 0.270) and also reduced the strength of the damping for horizontal component of turbulent energy (clubb_$c14$ = 2.2 → 1.6) to increase cloudiness. For a description of how CLUBB parameters impact the simulated climate, see Guo et al. (2015).

2.3. Grids

We evaluate model simulations on six different grids in this study (Table 1). The FV dycore is run with nominal 1° and 2° grid spacing, referred to as f09 and f19, respectively (Figures 1a and 1b). We also run the 1° equivalent of the SE-CSLAM grid, referred to as ne30pg3 (Figure 1d), where *ne* refers to a grid with *ne* × *ne* quadrilateral elements per cubed-sphere face, and *pg* denotes that there are *pg* × *pg* control volumes per element for computing the physics. We run an additional 1° SE-CSLAM simulation with the physical parameterizations computed on a grid with 2 × 2 control volumes per element, ne30pg2 (Figure 1c; Herrington et al., 2019, note CSLAM is still run on the 3 × 3 control volume grid).

Three VR meshes were developed for the CESM2.2 release to support grid refinement over the Arctic and the United States (Figure 2). This paper serves as the official documentation of these grids. The VR meshes were developed using the software package SQuadgen (https://github.com/ClimateGlobalChange/squadgen). The Arctic grid is a 1° grid with 1/4° regional refinement over the broader Arctic region (when using degrees to describe the resolution of unstructured grids, we refer to degrees at the equator). The Arctic − GrIS grid is identical to the Arctic grid, but with an additional patch covering the island of Greenland with 1/8° resolution. The CONUS grid contains 1/8° refinement over the United States, and 1° everywhere else. The CONUS grid is not discussed any further in this paper; see Pfister et al. (2020) for simulations with the CONUS grid.

The accuracy of the simulated surface mass balance is expected to be sensitive to grid resolution. Figure 3a shows the average grid spacing over the Greenland Ice Sheet (*GrIS* hereafter) in all six grids, as well as two grids pertaining to the Regional Atmospheric Climate Model (RACMO; Noël et al., 2018, 2019), which are used for validation (Table 2). The ne30pg2 grid has the coarsest representation with an average grid spacing (Δx) of Δx = 160 km, and the Arctic − GrIS grid has the highest resolution with an average grid spacing of Δx = 14.6 km, similar to the 11 km grid spacing of the RACMO2.3 grid. The ne30pg3 grid has an average Δx = 111.2 km, substantially coarser than the f09 grid, with an average Δx = 60 km. Although ne30pg3 and f09 have similar average grid

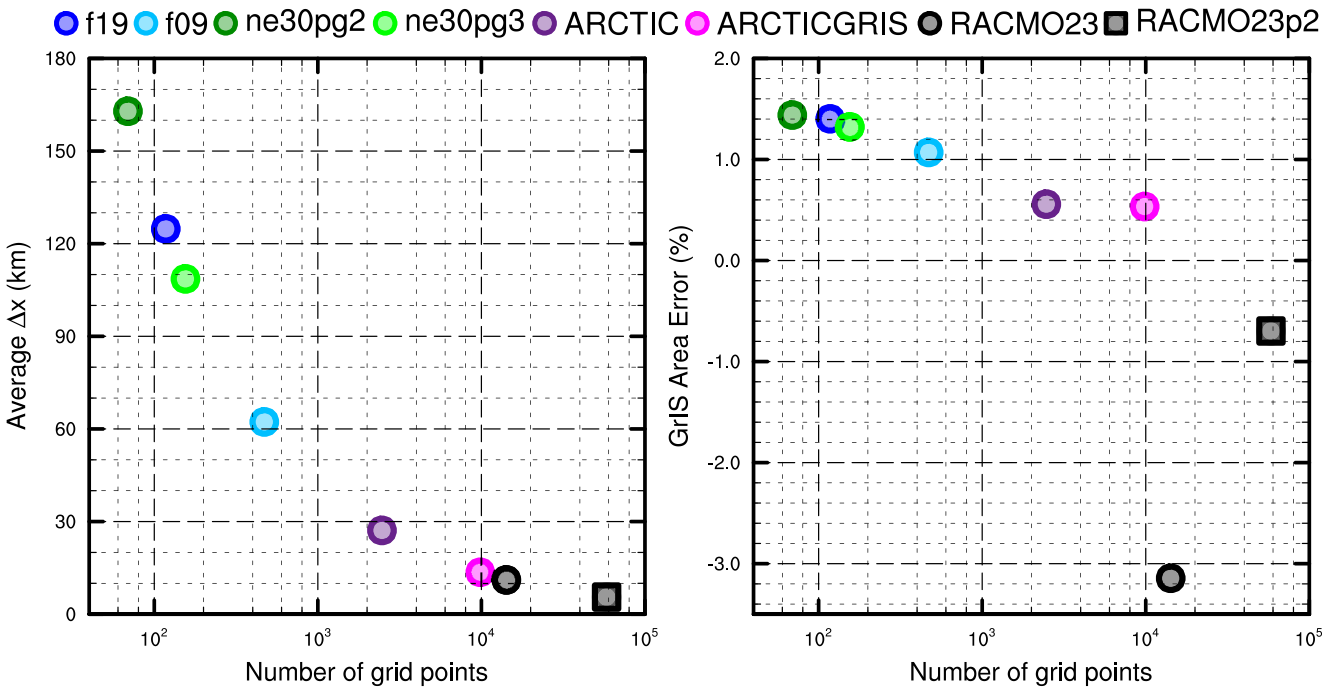

Figure 3. The spatial properties of the GrIS as represented by different grids in this study. (Left) approximate average grid spacing over GrIS, (right) GrIS area error, computed as the relative differences from the reference data set described in the text. Also included are the two RACMO grids used for validation (see Table 2).

spacing over the entire globe, and comparable computational costs (Table 1), the convergence of meridians on the FV grid enhances the resolution over the GrIS. The Arctic grid has an average grid spacing of $\Delta x = 27.8$ km.

The physics time step depends on the grid resolution. Increased horizontal resolution permits faster vertical velocities that reduce characteristic time scales, so the physics time step is reduced to avoid large time truncation errors (Herrington & Reed, 2018). The Arctic and Arctic – GrIS grids are run with a 4× and 8× reduction in physics time step relative to the default 1,800 s time step used in the 1° and 2° grids (Table 1).

All grids and dycores in this study use 32 hybrid pressure-sigma levels in the vertical, with a model top of 2 hPa or about 40 km. However, any grid or dycore can in principle be run with a higher model top or finer vertical resolution.

2.4. Computational Costs

The last columns of Table 1 provide cost estimates for the different grids and dycores. The costs, expressed as core hours per simulated year (CHPSY), are taken from single-month runs of FHIST, with no i/o, and using 25 nodes (900 tasks) and 50 nodes (1,800 tasks) on the Cheyenne supercomputer (Computational and Information Systems Laboratory, 2017). For a typical multi-decadal climate simulation at 1° resolution, 25 nodes are on the

Table 2
Description of Validation Data Sets Used in This Study

Data product	Years used in this study	Resolution	Citation
ERA5	1979–1998	1/4°	Copernicus (2019)
CERES-EBAF ED4.1	2003–2020	1°	Loeb et al. (2018)
CALIPSO-GOCCP	2006–2017	2°	Chepfer et al. (2010)
MODIS-MAR	2000–2013	25 km	Tedesco and Alexander (2013)
RACMO2.3	1979–1998	11 km	Noël et al. (2015)
RACMO2.3p2	1979–1998	5.5 km	Noël et al. (2019)

low side. However, this is the largest number of tasks supported by the f19 grid, and we fixed the number of tasks across all grids for the purpose of comparing costs. We also show costs for 50 nodes, excluding f19, to provide a more practical estimate for longer climate integrations. Other approaches for comparing costs across different grids and dycores, for example, holding fixed the number of grid columns per task, are beyond the scope of this study.

The cheapest grid is the f19 grid at 436.66 CHPSY, as this is the only grid with 2° dynamics. The f09 grid costs 1534.57 CHPSY using 25 nodes, which is noticeably cheaper than ne30pg3 at 1890.48 CHPSY. The ne30pg2 grid is 20% cheaper than the ne30pg3 grid, in both the 25 node and 50 node runs, consistent with previous estimates (Herrington & Reed, 2018). The FV model is known to be cheaper than SE at small core counts, whereas SE is more efficient than FV at large core counts due to its improved scalability (Dennis et al., 2005, 2012). In the more conventional 50-node runs, f09 costs are more similar to ne30pg3, due to a 30% cost increase in f09 relative to the 25-node run (Table 1). The Arctic grid is an order of magnitude more expensive than the lat-lon and quasi-uniform grids, at about 16k CHPSY, whereas the Arctic – GrIS grid adds another factor of ∼2 (40k CHPSY). All timing numbers are from runs without threading. The f09 grid is the only grid that runs out-of-the-box with threading; holding the number of tasks fixed reduces CHPSY by 4%–6.5% reduction compared to runs without threading.

2.5. Simulated Surface Mass Balance (SMB)

CESM simulates the GrIS SMB as the sum of ice accumulation and ice ablation. The latter includes sublimation, as well as liquid runoff from ice melt. Liquid precipitation and runoff may also contribute to ice accumulation by penetrating pore spaces in the snowpack/firn layer and freezing, forming ice lenses. The relevant SMB processes are represented by different CESM components, but it is the Community Land Model, version 5 (CLM; Lawrence et al., 2019), that aggregates these processes and computes the SMB.

CLM runs on the same grid as the atmosphere, and uses a downscaling technique to account for sub-grid variability in SMB. In short, the ice sheet patch in a CLM grid cell is subdivided into 10 elevation classes (ECs), each with a distinct surface energy balance and SMB. The area fraction of each EC is computed from the CISM initial conditions, which are based on a high-resolution data set of the observed, modern extent and thickness of the GrIS (Morlighem et al., 2014). For configurations with a dynamically active ice sheet, the area fractions are continuously updated throughout the run to reflect the evolving ice sheet geometry in CISM. The near-surface air temperature, humidity, and air density are calculated for each EC using an assumed lapse rate and the elevation difference from the grid-cell mean. Precipitation from CAM is repartitioned into solid or liquid based on the surface temperature of the EC; precipitation falls as snow for temperatures between $T < -2°C$, as rain for $T > 0°C$, and as a linear combination of rain and snow for temperatures between −2° and 0°C.

Changes in ice depth, not snow depth, count toward the SMB. Snow accumulation in each EC is limited to a depth of 10 m liquid water equivalent. Any snow above the 10 m cap contributes to ice accumulation, and refreezing of liquid water within the snowpack is an additional source of ice. Surface ice melting (after melting of the overlying snow) yields a negative SMB. Integrating over all ECs, weighting by the area fractions, provides a more accurate SMB than would be found using the grid-cell mean elevation. For a more detailed description of how the SMB is computed in CESM, we refer the reader to Lipscomb et al. (2013), Sellevold et al. (2019), van Kampenhout et al. (2020), and Muntjewerf et al. (2021).

Since snow in the accumulation zone must reach the cap to simulate a positive SMB, the snow depths on the VR grids were spun up by forcing CLM in standalone mode, cycling over data from a 20-year Arctic FHIST simulation (with perpetual 1979 boundary conditions) for about 500 years. The 1°–2° lat-lon and quasi-uniform unstructured grids are initialized with the SMB from an existing f09 spun-up initial condition.

2.6. Validation Data Sets

We use several validation data sets (Table 2) to assess the performance of the simulations. The ERA5 reanalysis product (Copernicus, 2019) is used to validate the large-scale circulation and extreme precipitation events. Clouds and radiation fields are validated using remote sensing products, the CERES-EBAF ED4.1 (Loeb et al., 2018) and

the CALIPSO-GOCCP (Chepfer et al., 2010) data sets, respectively. We also use a MODIS GrIS surface albedo product, mapped to a 25 km regional climate model grid (Tedesco & Alexander, 2013).

SMB data sets are gathered from multiple sources. RACMO, version 2.3 11 km (RACMO23; Noël et al., 2015) and version 2.3p2 5.5 km (RACMO2.3p2; Noël et al., 2018, 2019) are RCM simulations targeting Greenland, forced by ERA renalyses products at the domain's lateral boundaries. The RACMO simulations have been shown to perform skillfully against observations and are often used as modeling targets (e.g., Evans et al., 2019; van Kampenhout et al., 2020). The RACMO data sets are used along with the CERES-EBAF product to validate the radiative fluxes around Greenland.

In-situ SMB (snow pit and ice cores) and remote sensing data sets (e.g., IceBridge radar accumulation data set) are maintained in The Land Ice Verification and Validation toolkit (LIVVkit), version 2.1 (Evans et al., 2019). However, these point-wise measurements are difficult to compare to model output spanning several different grids, especially since the SMB from each elevation class is not available from the model output. We used a nearest-neighbor technique for an initial analysis, which showed that the model biases are similar to those computed using the RACMO data sets. Because of the uncertainty of comparing gridded fields to point-wise measurements, and the lack of information added with regard to model biases, we omitted these data sets from our analysis.

2.7. SMB Analysis

We seek to integrate SMB components over a GrIS ice mask and to diagnose their contributions to the GrIS mass budget. However, the ice masks vary across the grids, especially in comparison to the RACMO3.2 ice mask, whose total area is about 3% less than that of the reference data set (i.e., the GrIS initial conditions in CISM; Figure 3b). CLM's data set creation tool generates the model ice mask by mapping the reference data set to the target grid using the Earth System Modeling Framework (ESMF) first-order conservative remapping algorithm (Team et al., 2021). The figure suggests that the mapping errors are less than 1.5% across the CESM2.2 grids. The area errors in Figure 3b may seem small, but even 1–2% area differences can lead to large differences in integrated SMB (Hansen et al., 2022).

We have taken a common-ice-mask approach by mapping all model fields to the lowest-resolution grids, that is, the `f19` and `ne30pg2` grids, and integrating over these low-resolution ice masks. The use of low-resolution common ice masks is a conservative decision, and is justified because we seek to use first-order remapping algorithms to map fields to the common ice mask, which is not generally reliable when mapping to a higher-resolution grid than the source grid. We use two remapping algorithms: ESMF first-order conservative and the TempestRemap (Ullrich & Taylor, 2015) high-order monotone algorithm. Since mapping errors are sensitive to grid type, we evaluate all quantities on both common ice masks, the `f19` and `ne30pg2` masks. Thus, we evaluate an integrated quantity on a given grid up to four times to estimate the uncertainty due to differences in grid type and remapping algorithms.

The SMB is expressed in a form that is agnostic of water phase, a total water mass balance, to facilitate comparisons across different grids with different ice masks and to increase consistency with the variables available in the RACMO data sets. The SMB for total water can be expressed as:

$$\mathtt{SMB} = \text{accumulation} + \mathtt{runoff} + \text{evaporation} + \text{sublimation}, \tag{1}$$

where all terms have consistent sign conventions (positive values contribute mass, and negative values reduce mass). The accumulation source term refers to the combined solid and liquid precipitation, runoff refers to the liquid water sink, and evaporation/sublimation is the vapor sink. Since the runoff term aggregates many processes, we isolate the melting contribution by also tracking the combined melt of snow and ice.

The total water SMB (Equation 1) is different from the SMB internally computed by CLM and described in Section 2.5, which only tracks ice mass. We do not use CLM's internally computed SMB in this study. Rather, we use the components of the internally computed SMB to construct the total water SMB.

We consider two approaches for mapping and integrating the SMB components over the common ice masks:

1. Map the grid-cell mean quantities to the common grid, and integrate the mapped fields over the common ice masks.
2. Map the patch-level quantities (i.e., the state over the ice fractional component of the grid cell) to the common grid, and integrate the mapped fields over the common ice masks.

Note that we are mapping to low-resolution grids that have larger GrIS areas than the source grids (Figure 3b). Since the components of Equation 1 are not confined to the ice mask, method 1 reconstructs the SMB over the portion of the common ice mask that is outside the ice mask on the source grid. While this may be a an acceptable way to reconstruct the mass source terms over different ice masks, ice melt is zero outside the source ice mask, and so method 1 will underestimate the mass sink term. This underestimation is systematic in method 2, where all variables are exclusive to the ice mask; mapping to a lower-resolution grid will dilute a field of non-zero values over the ice mask with a field of zeros outside the ice mask. However, patch-level values for processes exclusive to the ice mask (e.g., ice melt) will on average have larger magnitudes than the grid-mean quantities used in method 1.

The different error characteristics of the two methods are used to further diversify the ensemble. Each of the four regridding combinations (with conservative and high-order remapping to the f19 and ne30pg2 grids) are repeated with each method, resulting in (up to) eight values for each integrated quantity. Unfortunately, the patch-level values of evaporation/sublimation are not available from the model output, and we estimate their contribution by zeroing out the field for grid cells that have no ice, prior to mapping to the common ice mask. This will degrade the SMB estimates using method 2, but we are more interested in characterizing the behavior of individual processes across grids and dycores, expressed as the components of the SMB, rather than the SMB itself.

3. Results

3.1. Tropospheric Temperatures

Before delving into the simulated Arctic climate conditions, we assess the global mean differences between the various grids and dycores. Figure 4 shows 1979–1998 annual mean, zonal mean height plots of temperature, expressed as differences between 1° and 2° lat-lon and quasi-uniform unstructured grids and dycores. The f09 grid is warmer than the f19 grid, primarily in the mid-to-high latitudes throughout the depth of the troposphere. This is a common response to increasing horizontal resolution in GCMs (Pope & Stratton, 2002; Roeckner et al., 2006). Herrington and Reed (2020) have shown that this occurs in CAM due to higher resolved vertical velocities which, in turn, generate more condensational heating in the CLUBB macrophyiscs. The right panel in Figure 4a supports this interpretation, showing an increase in the climatological CLUBB heating at all latitudes in the f09 grid, but with the largest increase in the mid-latitudes.

As the SE dycore is less diffusive than the FV dycore, the resolved vertical velocities are larger in the SE dycore, and so the ne30pg3 troposphere is modestly warmer than f09 (Figure 4b). The stratosphere responds differently, with ne30pg3 much cooler than f09 in the mid-to-high latitudes. Figure 4c also shows small temperature differences between ne30pg3 and ne30pg2, with ne30pg3 slightly warmer near the tropopause at high latitudes. This is consistent with the similar climates found for these two grids by Herrington et al. (2019).

Comparing the VR grids to the lat-lon and quasi-uniform grids is complicated because we simultaneously increase the resolution and reduce the physics time-step, both of which influence the solution (Williamson, 2008). We therefore run an additional ne30pg3 simulation with the shorter physics time step used in the Arctic grid (450 s), referred to as ne30pg3* (Table 1). Figure 5a shows the difference between ne30pg3* and ne30pg3 for climatological summer temperatures in zonal-mean height space. The troposphere is warmer with the reduced time step, and the mechanism is similar in that the shorter time step increases resolved vertical velocities (not shown) and CLUBB heating (right panel in Figure 5a). Figure 5b shows the difference in climatological summer temperature between the Arctic grid and the ne30pg3* grid. With the same physics time step, the greater condensational heating and warmer temperatures are confined to the refined Arctic region.

There is not perfect alignment of the CLUBB heating anomalies and the temperature anomalies in Figures 4 and 5. This leaves some uncertainty as to whether CLUBB is solely responsible for the temperature anomalies

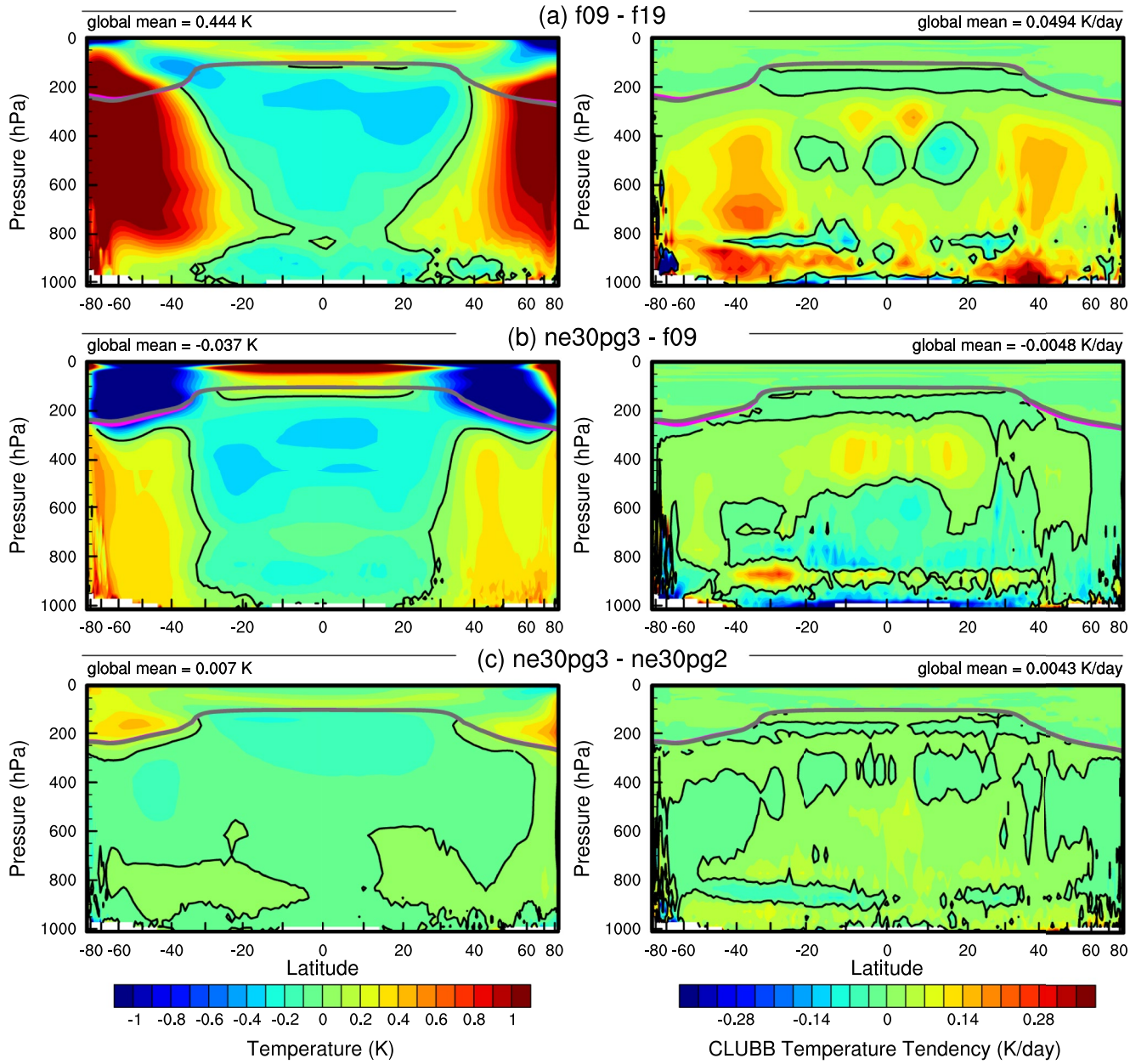

Figure 4. 1979–1998 annual mean temperature (left column) and CLUBB temperature tendencies (right column) in zonal mean height space, expressed as differences between the various 1°–2° grids. The thick gray and magenta lines are the tropopause for the control run and the test run, respectively.

caused by changing grid resolution or dycore, as asserted above. In the deep tropics, gravity waves are expected to propagate temperature anomalies far from their heating source, and so some misalignment is expected for this region. In the mid-latitudes, we speculate that the misalignment is due to averaging the CLUBB heating over all time. Herrington and Reed (2020) have shown that only the CLUBB heating coinciding with upward resolved vertical velocities tends to align spatially with the temperature response, whereas heating anomalies associated with descending grid columns have no alignment with the temperature response. Therefore the average over all time will dilute the heating signal, potentially leading to misalignments.

Figure 5c shows that the Arctic – GrIS grid is much warmer than the Arctic grid in the Arctic summer. This may be due, in part, to the shorter physics time step, but the temperature response is too large to be explained by enhanced condensational heating from CLUBB alone. This summer warming appears to be a result of variations in the stationary wave pattern, with a swath of anomalous southerly winds to the west of Greenland (not shown).

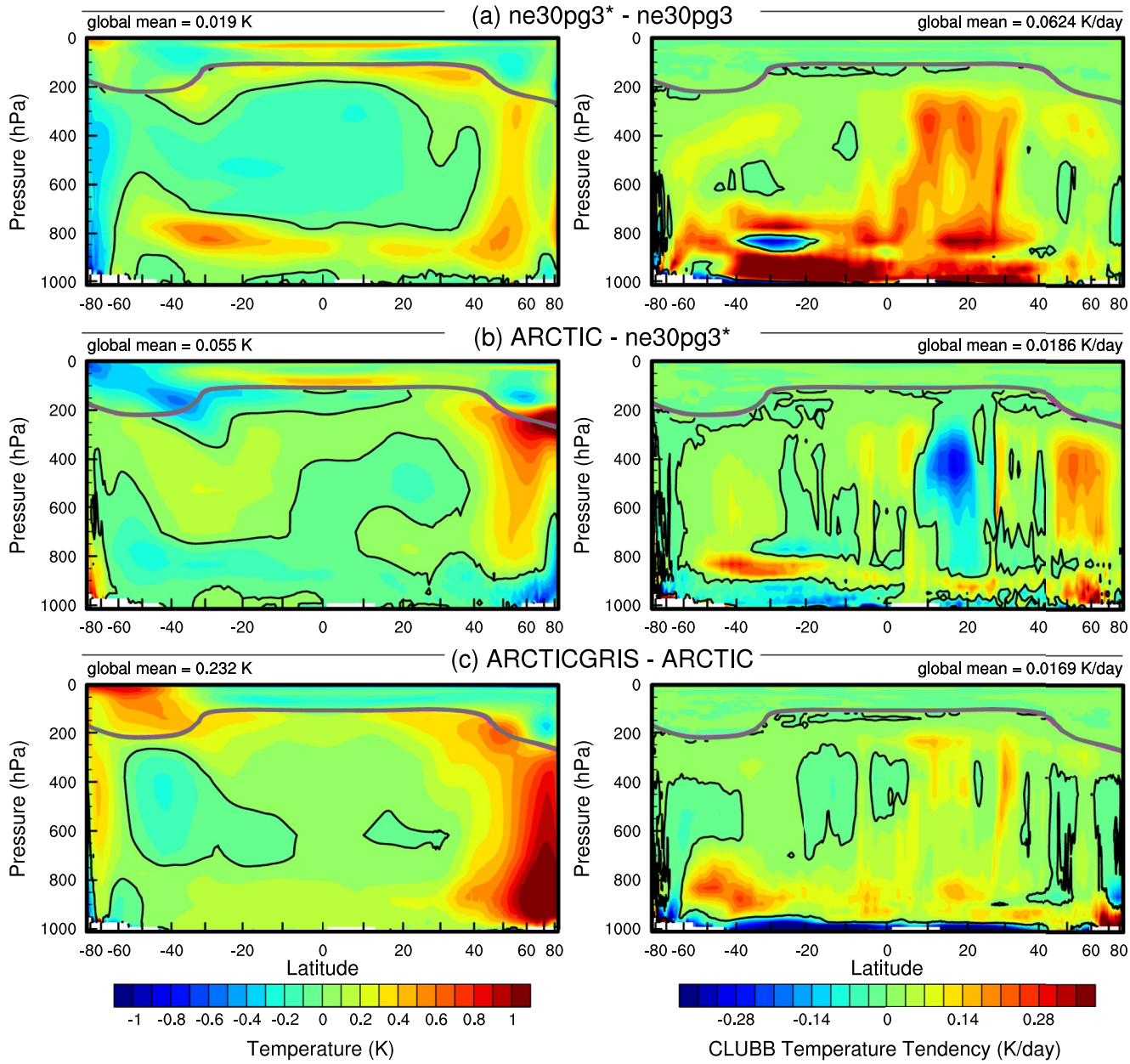

Figure 5. As in Figure 4 but for the short-time-step experiment and the VR grids. The fields plotted are for the climatological northern hemisphere summer. We focus on summer because that is when the resolution response is largest, and the refined regions are located in the northern hemisphere.

This dynamic response is interesting, because other than the physics time step, the only difference between the `Arctic` − GrIS and `Arctic` runs is the doubling of resolution over Greenland. This behavior will be explored further in a future study.

Keeping our focus on the Arctic region, and in particular Greenland, it is useful to understand summer temperature biases due to their control on ice and snow melt over the GrIS (Ohmura, 2001). Figure 6 shows the 1979–1998 lower-troposphere summer temperature bias relative to ERA5, computed by equating a layer mean virtual temperature with the 500–1,000 hPa geopotential thickness. The results are consistent with the zonal mean height plots; increasing resolution from `f19` to `f09` warms the climate, and the 1° SE grids are warmer than the FV grids. The FV summer temperatures are persistently colder than ERA5, whereas the 1° SE grids are not as cold, and are actually warmer than ERA5 at high-latitudes, north of 75°. All grids show a north-south gradient in bias over

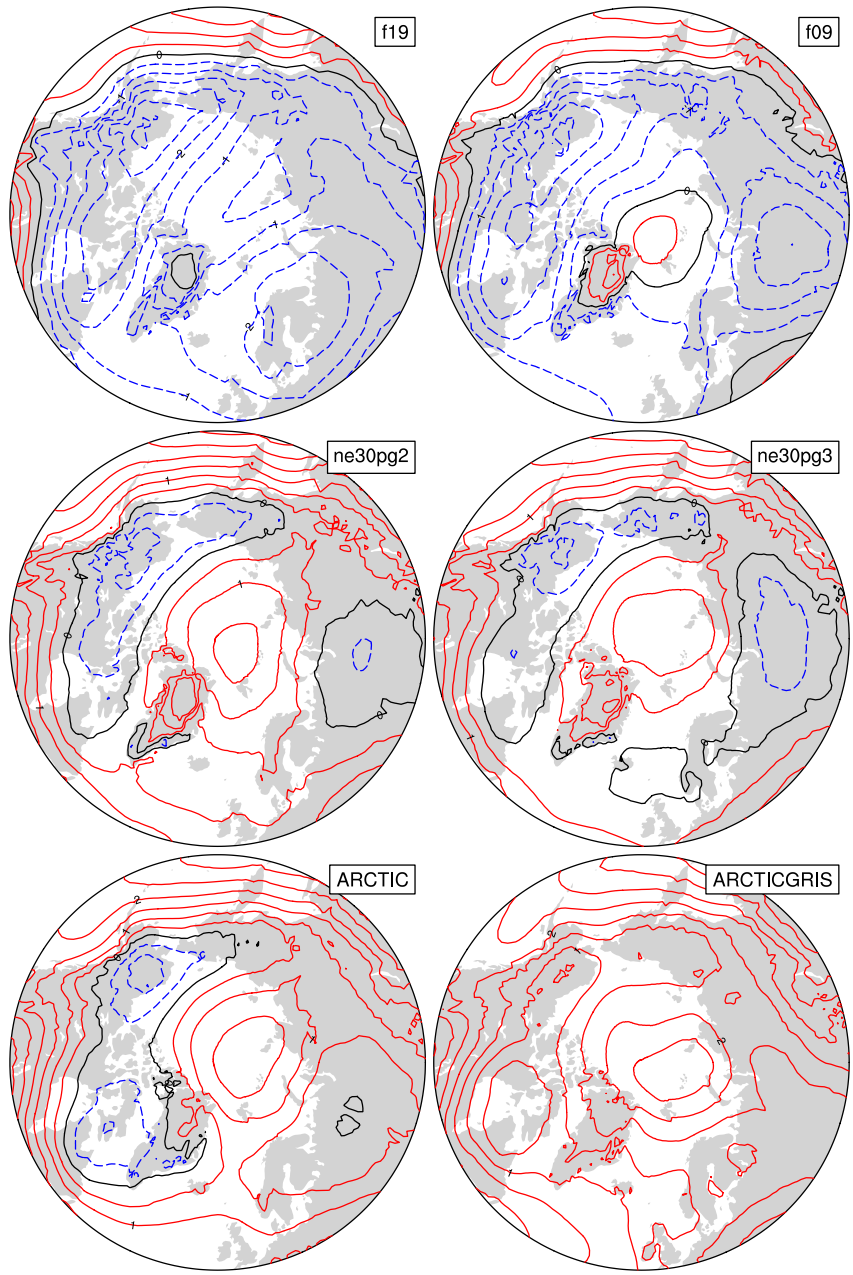

Figure 6. 1979–1998 lower troposphere, northern hemisphere summer virtual temperature biases, computed as the difference from ERA5. Lower troposphere layer mean virtual temperature is derived from the 1,000–500 hPa geopotential thickness, using the hypsometric equation. Differences are computed after mapping the ERA5 data to the finite-volume grids since the geopotential field is only available on the output tapes in the spectral-element runs that have been interpolated to the `f09` grid, inline.

Greenland, with the summer temperature bias more positive for the northern part of the ice sheet. This pattern is also evident in the near-surface temperature bias over Greenland (not shown).

The `Arctic` grid has summer temperatures similar to the 1° SE grids, but is slightly warmer over northern Eurasia and the North Pole (Figure 6). An anomalous cooling patch forms to the west of Greenland, centered over Baffin Island. The `Arctic – GrIS` grid is warmer than the `Arctic` grid over most of the Arctic, but with a similar spatial pattern of summer temperature bias.

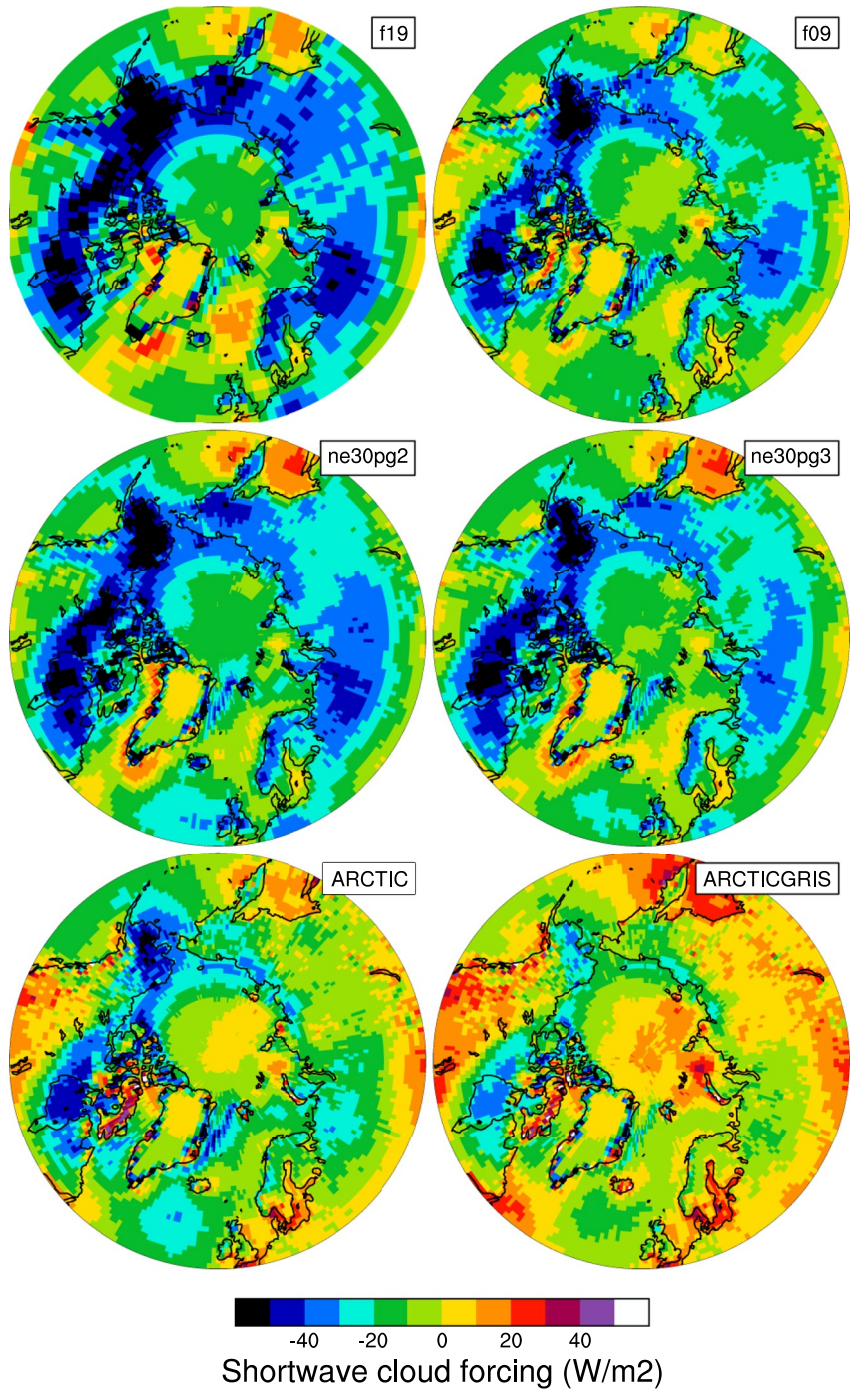

Figure 7. 1979–1998 Northern Hemisphere summer shortwave cloud forcing bias, relative to the CERES-EBAF gridded data set. Shortwave cloud forcing is defined as the difference between all-sky and clear-sky net shortwave fluxes at the top of the atmosphere. Differences are computed after mapping all model output to the 1° CERES-EBAF grid.

Some of these temperature differences may be related to differences in summer cloudiness. Figure 7 shows the summer shortwave cloud forcing bias in the six runs, using the CERES product. Shortwave cloud forcing quantifies the impact of clouds on shortwave radiation, taken as the difference between all-sky and clear-sky shortwave radiative fluxes at the top of the atmosphere. A negative bias corresponds to excessive reflection and cooling. The lat-lon and quasi-uniform grids have similar biases, with the clouds reflecting 20–40 W/m^2 too much shortwave radiation over a wide swath of the Arctic, primarily the land masses. There is also a halo of positive bias

(clouds not reflective enough) around the ocean perimeter of Greenland. The Arctic grid has much smaller cloud forcing biases over the Arctic land masses, but is still too reflective over Alaska, the Canadian Archipelago, and parts of Eurasia. Compared to the Arctic grid, the Arctic − GrIS grid vastly reduces the cloud forcing bias over Eurasia, and also improves the bias over North America. In both VR grids, the halo of positive shortwave cloud forcing bias around the perimeter of Greenland is absent.

The summer cloud forcing biases are consistent with the summer temperature biases in Figure 6—regions where clouds are too reflective coincide with regions that are too cold. While we have not quantified the contribution of cloud biases to the cooler Arctic temperatures, shortwave radiation is a crucial component of the Arctic energy budget during summer. The shortwave cloud forcing biases are on the order of 10 W/m2, which is a significant fraction of the total absorbed shortwave radiation during Arctic summer (Serreze et al., 2007) and is therefore likely a factor contributing to the cooler temperatures.

3.2. Clouds and Precipitation Over Greenland

In addition to summer temperatures, shortwave radiation is an important determinant of snow and ice melt. Figure 8 shows the summer incident shortwave radiation bias at the surface over Greenland and surrounding seas. The top panel shows the bias relative to the RACMO2.3p2 data set, and the middle panel relative to the CERES data set. The halo of excessive incident shortwave radiation around the coasts of Greenland is apparent for both data sets in relation to the coarser grids, consistent with the shortwave cloud forcing biases in Figure 7.

The ice sheet interior receives too little shortwave radiation in the coarser grids. On the VR grids, both the interior shortwave deficit and the excessive shortwave around the ocean perimeter are improved. This suggests that the coarse-grid clouds are too thick in the interior of Greenland and too thin around the perimeter, which is consistent with the total summer cloud fraction bias, computed from the CALIPSO cloud data set and shown in the bottom panel of Figure 8. Note that total cloud fraction characterizes the cloud field at all vertical levels, and attenuates the changes arising from any single layer due to the occurrence of overlapping clouds at other levels. The VR grids exhibit an overall improvement in total cloud fraction bias, relative to the coarse grids.

The top panel of Figure 9 shows the annual climatological mean precipitation bias over the GrIS, expressed as the fractional difference from the RACMO2.3p2 solution. The coarse 1°–2° grids have large, positive biases centered over the southern dome. The Arctic grid reduces this bias substantially, and the Arctic − GrIS grid reduces it further, with precipitation centers migrating from the interior toward the margins.

The more accurate representation of orographic precipitation in the VR grids is consistent with the cloud and radiation biases, cf. Figures 7–9. The agreement of the cloud, radiation and precipitation biases in and around Greenland from multiple independent data sets indicates that the biases are a robust feature of the coarser grids. The reduced biases in the VR grids suggest that the deficiencies of the coarse grids are due to insufficient horizontal resolution, consistent with previous findings that coarse GCMs have large, positive precipitation biases over Greenland (Pollard & Groups, 2000; Van Kampenhout et al., 2019).

3.3. Greenland Surface Mass Balance

Table 3 shows the 1979–1998 climatological SMB components for each grid, compared with RACMO. The values in the table are averages over the ensemble of mapping methods to the common ice masks described in Section 2.7, and the RACMO values refer to the average of both RACMO ensembles. Table 3 also contains (in parenthesis) the SMB components derived from evaluating the integrals on each model's native grid and ice mask. For the accumulation term in the quasi-uniform SE grids, the native grid values are actually less than common ice mask values, likely due to the inflationary impacts of method 1 discussed in Section 2.7. For the total melt term, the common ice mask values aren't nearly as dissipative as expected, with only the Arctic − GrIS grid showing a large reduction in melt rates relative to the native grid values.

The coarse grids are characterized by too much precipitation and too much melting and runoff, compared with RACMO. The total SMB on coarse grids therefore has smaller errors than the individual components (Table 3), because large errors in the source and sink terms offset one another when added together. Such compensating errors underscore the importance of understanding whether a model is getting the right SMB for the right reasons.

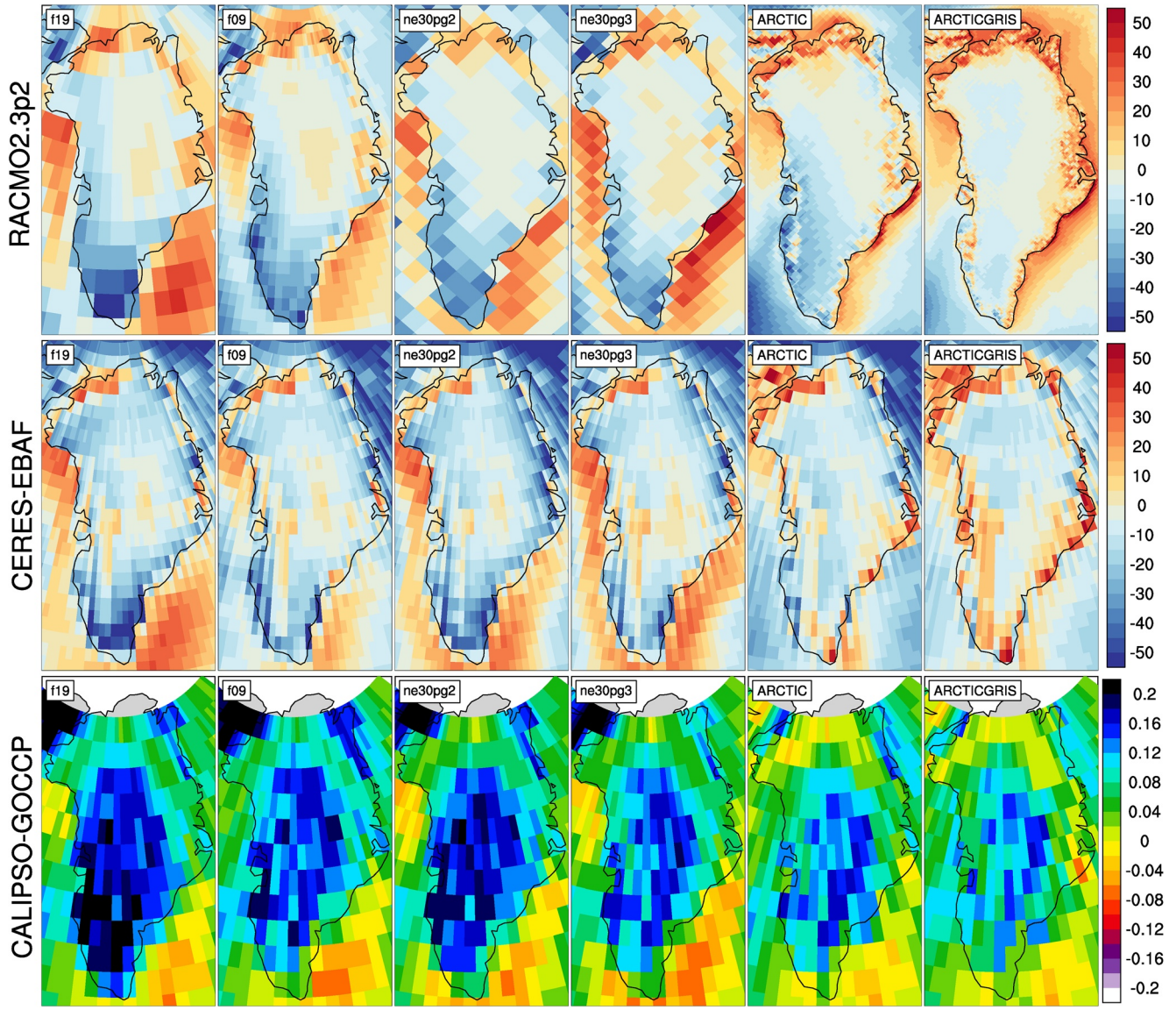

Figure 8. 1979–1998 northern hemisphere summer surface incident shortwave radiation bias (W/m2), computed as the difference (top) from RACMO2.3p2, and (middle) the CERES-EBAF data set, and the (bottom) total cloud fraction bias relative to the CALIPSO data set. CERES and CALIPSO differences are found by mapping the model output to their 1° and 2° grids, respectively, and differences in the bottom panel are computed after mapping the RACMO2.3p2 data set to the individual model grids. Note that the averaging period for the CALIPSO-GOCCP and CERES-EBAF panels, 2006–2017 and 2003–2020, respectively, are different from the averaging period for the model results.

Figure 10 shows time series of annually integrated precipitation and snow/ice melt over the GrIS for the various different grids and dycores, and RACMO in black. The 1979–1998 climatological mean values from Table 3 are shown as circles on the right side of the panels. The 1°–2° lat-lon and quasi-uniform grids have positive precipitation biases, whereas the VR grids have the smallest biases, with precipitation comparable to RACMO. The `f19` and `f09` grids perform similarly, with +200 Gt/yr bias, whereas `ne30pg3` is biased by about +250 Gt/yr and `ne30pg2` by +330 Gt/yr.

The combined annual snow/ice melt shown in the bottom panel of Figure 10 indicates that the `Arctic` grid simulates the most realistic melt rates, with the other grids having more melt than RACMO. The `Arctic` − GrIS grid over-predicts melting by about 150 Gt/yr. This is likely due to an anomalously warm lower troposphere during the summer, relative to the `Arctic` run (Figure 6). The `f19` and `f09` melting rates are improved over `Arctic` − GrIS,

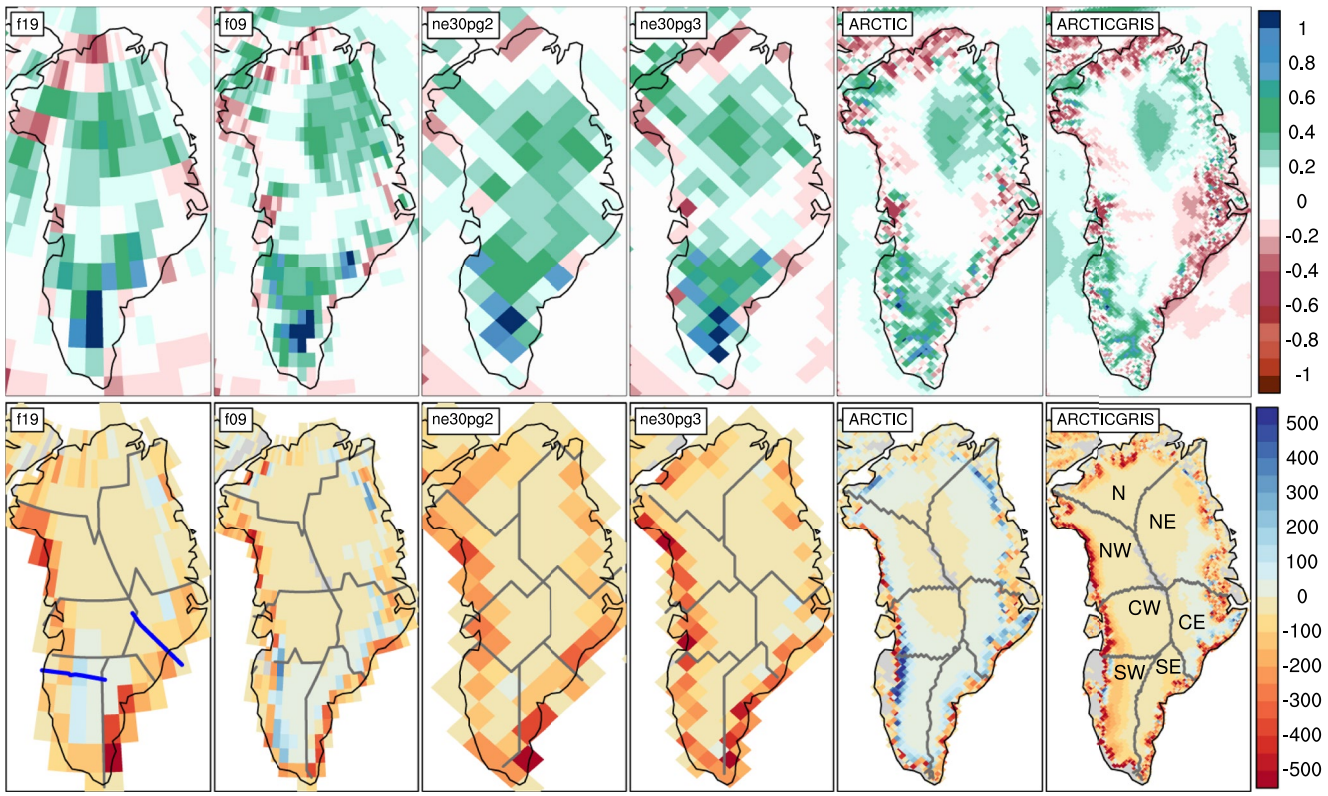

Figure 9. 1979–1998 (top) annual precipitation and (bottom) ice/snow melt biases relative to RACMO2.3p2, evaluated on the native model grids. The precipitation biases are expressed as fractional changes, whereas the melt biases are absolute changes (mm/yr). In the bottom panel, the Rignot and Mouginot (2012) basin boundaries are shown in gray for each model grid. Note that Figure 11 uses the basin boundaries for the two common ice masks, shown in the f19 and ne30pg2 panels, in computing the basin-scale integrals. Blue lines in the f19 panel show the location of the two transects plotted in Figure 12.

overestimating melt by only 100–120 Gt/yr. The SE grids have the largest positive melt bias, between 240 and 265 Gt/yr.

To illustrate the regional behavior of the SMB components, Figure 11 shows the precipitation and combined snow/ice melt integrated over the basins defined by Rignot and Mouginot (2012). The uncertainty due to differences in basin area is larger than for GrIS-wide integrals, owing to the differences in basin boundaries on the common ice masks, which are shown in the f19 and ne30pg2 panels of Figure 9. Nonetheless, the regional totals in Figure 11 correctly show that the southeast and southwest basins have the most accumulation. In all basins, accumulation decreases monotonically with increasing grid resolution, though with some exceptions.

Table 3
1979–1998 Surface Mass Balance of the Greenland Ice Sheet in Gt/yr

Grid name	Accumulation	Total melt	Runoff	Evap + subl	SMB
RACMO	681.7 (733.5)	−318.6 (−436.4)	−189.1 (−258.5)	−34.5 (−38.8)	458.1 (436.2)
ne30pg2	1013.6 (986.9)	−560.6 (−561.4)	−410.0 (−380.6)	−39.0 (−37.2)	564.6 (569.1)
ne30pg3	930.6 (909.7)	−583.1 (−543.6)	−403.2 (−337.9)	−39.1 (−37.6)	488.3 (534.2)
f19	888.2 (919.7)	−446.3 (−472.1)	−304.5 (−307.6)	−41.9 (−42.9)	541.8 (569.2)
f09	878.6 (891.6)	−419.5 (−401.5)	−274.4 (−230.6)	−42.3 (−42.4)	561.9 (618.6)
Arctic	786.3 (823.5)	−361.2 (−350.5)	−231.4 (−199.1)	−47.0 (−48.7)	507.9 (575.7)
Arctic − GrIS	695.9 (751.6)	−471.6 (−513.7)	−297.7 (−301.8)	−53.2 (−57.0)	345.0 (392.8)

Note. Values shown are using the common ice mask approach described in the methods section, whereas values in parentheses are from integrating over the native grid and ice mask. Evap + subl refers to the combined evaporation and sublimation term.

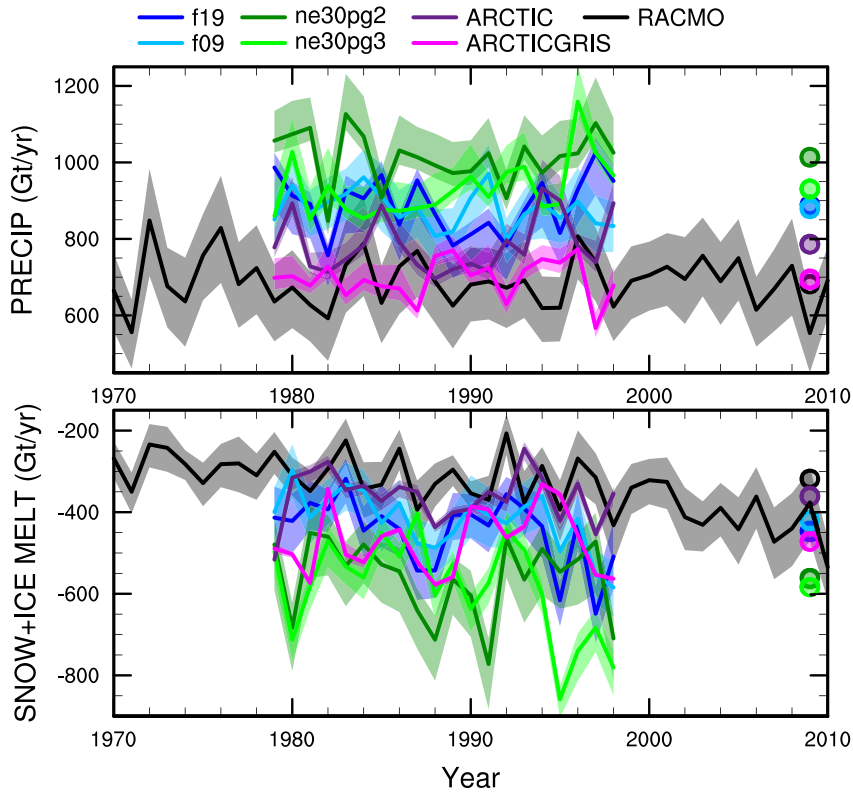

Figure 10. Time-series of annual (solid + liquid) precipitation (top) and annual runoff (bottom) integrated over the Greenland Ice Sheet for all six simulations and compared to the RACMO data sets. The time-series were generated using the common ice mask approach, which results in up to four ensembles, with the mean value given by the solid line and shading spanning the extent of the ensemble members.

The Arctic – GrIS grid simulates less precipitation than RACMO in the central-east and southeast basins, and is closest of all grids to RACMO in the large southwest basin.

The basin-integrated melt rates in Figure 11 depend on the dycore. The quasi-uniform SE grids have the largest positive biases in all basins. The Arctic – GrIS grid is a close second, while the FV grids have systematically smaller melt-rates and melt-rate biases. The "second-place" standing of Arctic – GrIS is somewhat unexpected, as this grid has the warmest lower-troposphere summer temperatures (Figure 6) and greatest incident shortwave radiation (Figure 8), yet it has less melting than the quasi-uniform SE grids.

Lower-troposphere temperature is not a strict proxy for melting; for example, it may not capture microclimate effects as a result of a better representation of the low-elevation ablation zones. The Positive Degree-Day temperature-based melt index (PDD; Braithwaite, 1984), which accumulates the near-surface temperature in °C for days with temperature above freezing, is a more accurate proxy for melting. PDD is nonlinear in mean monthly temperature (Reeh, 1991). We compute PDD from monthly mean 2-m temperature using the method of Calov and Greve (2005), assuming a fixed monthly mean standard deviation of 3°C and a degree-day factor of 5 mm d^{-1} $°C^{-1}$. This specific degree-day factor lies between typical values reported for snow and ice, in order to apply the PDD method to estimate the combined snow and ice melt.

Figure 11c shows the basin-integrated PDD melt estimate. In the large southeast and southwest basins (and all the other western basins), the ne30pg3 grid has larger PDD-based melt than the Arctic – GrIS grid. The FV grids also have large PDD-based melt in the southwest basin, relative to Arctic – GrIS. The PDD plots indicate that the relationship between temperature and melt is not well approximated by the summer lower-troposphere temperatures in Figure 6.

The bottom panel of Figure 9 presents the biases in the combined ice/snow melt as map plots. These plots show that the largest melt biases are on the southeast and northwest coasts, where large coarse-grid cells overlap with

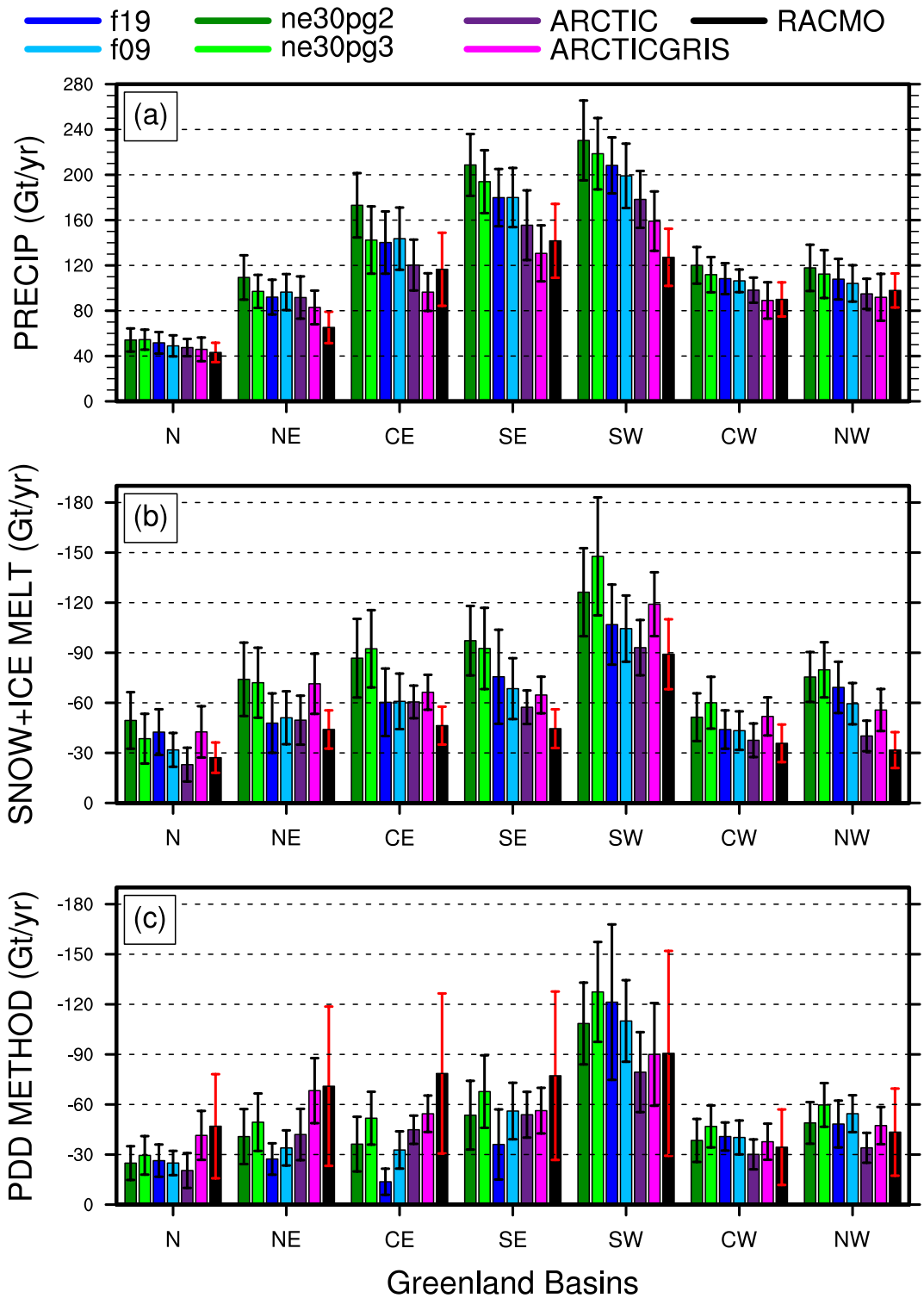

Figure 11. 1979–1998 basin integrated components of the SMB; (top) precipitation, (middle) ice/snow melt and (bottom) ice/snow melt estimated from the PDD method. Whiskers span the max/min of the four ensemble members generated from the common-ice-mask approach. Basin definitions are after Rignot and Mouginot (2012), and are found on the common ice masks using a nearest neighbor approach, and shown in Figure 9.

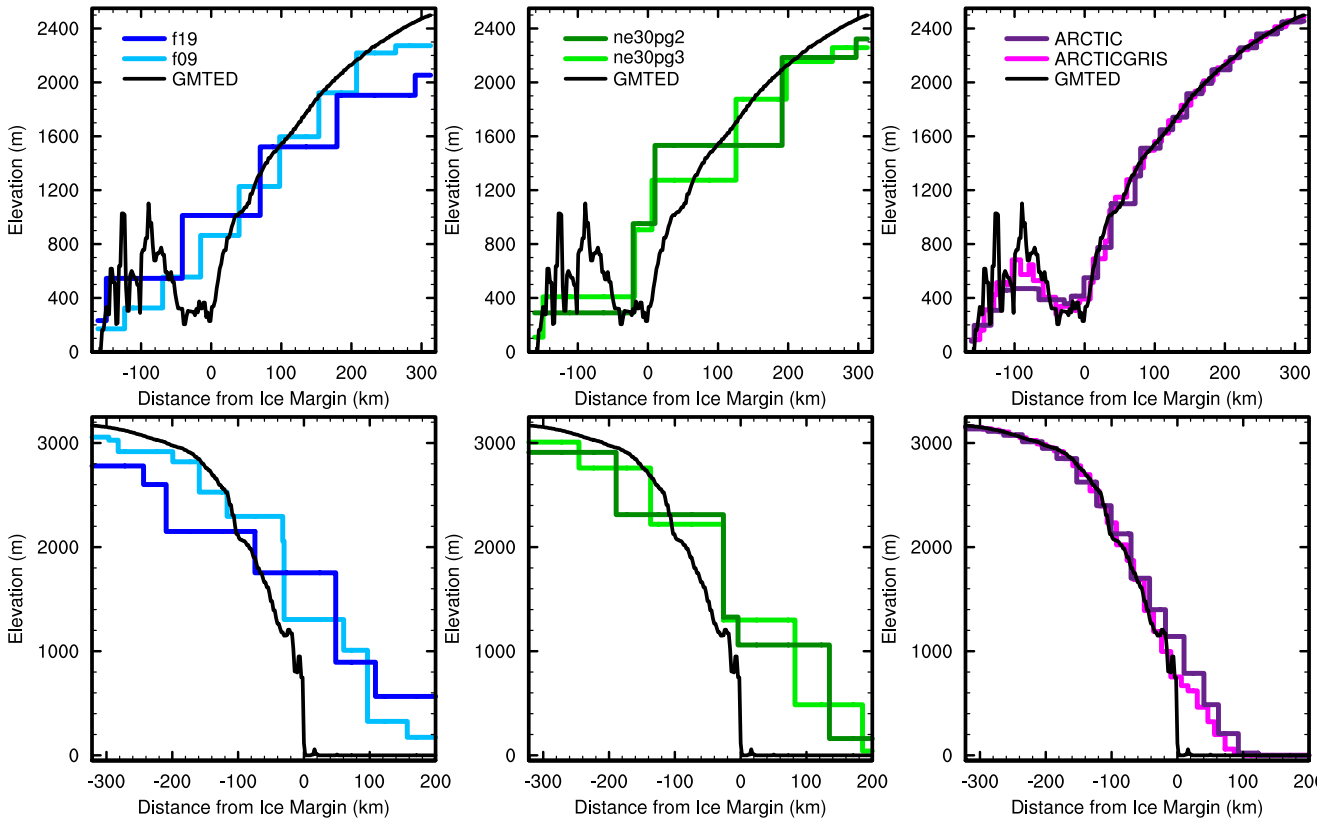

Figure 12. Model surface elevation along the (top) K-transect, and (bottom) a transect spanning the central dome down to the Kangerlussuaq glacier in southeast Greenland, for all model grids. The GMTED reference surface is a 1 km surface elevation data set (Danielson & Gesch, 2011) used for generating the CAM topographic boundary conditions.

the ocean. One possibility is that these problematic grid cells are situated at lower elevations than the true ice sheet surface, leading to a warm bias and too much melt. Figure 12 shows the representation of the ice sheet surface along two transects on the different grids, compared to the high-resolution data set used to generate CAM topographic boundary conditions (Danielson & Gesch, 2011; Lauritzen et al., 2015). The two transects are shown in Figure 9: the east-west "K-transect" in southwest Greenland and a transect extending from the central dome down to the Kangerlussuaq glacier on the southeast coast. The 1°–2° grids are noticeably coarse, with only a handful of grid cells populating the transect. The `f09` grid is a bit of an exception since the grid cells narrow in the zonal direction at high latitudes, and so more grid cells fit into the east-west transects. The VR grids more accurately reproduce the steep margins of the ice sheet, capturing the characteristic parabolic shape of the GrIS margin.

The transects in Figure 12 show that the ice sheet surface on the coarse grids is not systematically lower than the true surface in ablation zones. Rather, the smoothing and flattening of the raw topography, necessary to prevent the model from exciting grid-scale numerical modes, causes the lower-elevation ablation zones to extend beyond the true ice sheet margin, causing the modeled ablation zones (which must reside within the ice sheet mask) to be elevated relative to the actual ice surface. The `f19` grid has both the smoothest topography and the flattest ice sheet since its dynamics are coarsest, whereas the `f09`, `ne30pg2` and `ne30pg3` grids have similar dynamical resolution and use identical smoothing. This suggests that coarser models will tend to elevate the ablation zones relative to where they should be, which may be expected to cause anomalous (adiabatic) cooling and depressed melt rates. This is opposite the melt bias in the coarse grid simulations. Also, the EC downscaling should be able to correct for situations where model ice surface is elevated relative to the true ice surface, although for very large elevation differences or errors, the EC scheme may not be adequate.

Figure 12 also shows the ice margin boundary, illustrating that the ablation zone lies in a narrow horizontal band where the ice sheet rapidly plunges to sea-level. Due to this abrupt transition, coarse grids will commonly

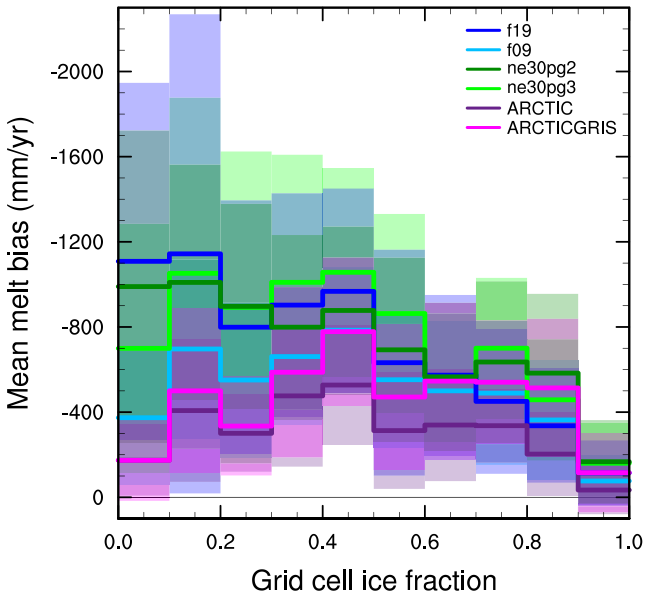

Figure 13. Average grid cell mean melt bias over the GrIS, computed relative to the RACMO data sets using the common ice mask approach, and conditionally sampled by grid cell ice fraction provided by the common ice masks. Solid lines are the mean of the distribution with ± one standard deviation expressed by shading.

represent the ablation zone with grid cells containing mixtures of ice-covered and ice-free regions. We hypothesize that coarser models have larger melt biases because summer melting is confined to these mixed ice/land/ocean grid cells. CLM deals with land heterogeneity in a complex and sophisticated manner, but CAM only sees the homogenized state after area-averaging over the sub-grid mixture. Thus, warm ice-free land patches in a grid cell may unduly influence the climate over the entire grid cell, causing a warm bias over the ice-covered patch and more melting.

Figure 13 shows the mean melt bias, relative to both RACMO data sets, conditionally sampled based on grid cell ice fraction in the GrIS region. Errors are computed after mapping the melt rates to the common ice masks using different methods, described in Section 2.7. The grid cell ice fractions therefore pertain to ice fractions on the low-resolution common ice masks. Also shown are the ±1 standard deviation of the biases for each bin. The figure shows that coarser grids can be characterized by a monotonic increase in melt bias as the grid cell ice fraction decreases. The VR grids have the smallest melt biases for small grid cell ice fractions (less than 50%), the quasi-uniform SE grids and `f19` have the largest melt biases, and the `f09` grid melt biases lie between these two cases. Figure 13 generally supports our hypothesis that the prevalence of mixed-grid cells in the ablation zone of coarse grids is responsible for their large melt bias.

Changes in surface albedo may also explain the melt differences in the grids and dycores. The top and middle rows of Figure 14 show maps of summer surface albedo biases in the simulations, relative to the RACMO2.3p2 and the processed MODIS albedo data set of Tedesco and Alexander (2013). The model surface albedo is diagnosed from the incident and net shortwave radiative fluxes at the surface. All grids and dycores have been mapped to the `f19` grid in the figure, and only cells overlapping with the `f19` GrIS ice mask are shown. Both RACMO2.3p2 and MODIS data sets indicate that the albedo in the quasi-uniform grids is lower in the central-west and northwest region, relative to the other grids, whereas the albedo is anomalously low at the southwest and southeast coastal margins in both lat-lon and quasi-uniform grids, compared with the VR grids. All grids and dycores have a positive albedo anomaly in northeast Greenland, which may explain the depressed melt rates and unrealistic ice sheet expansion in this region when coupled to the dynamic ice sheet (Lofverstrom et al., 2020).

The lower albedo values in the lat-lon and quasi-uniform grids is consistent with their larger melt rates. Since bare ice has a lower albedo than snow, lower snow fractions over the GrIS will expose larger areas of bare ice and reduce the surface albedo. The bottom panel of Figure 14 shows the summer snow fraction bias, computed relative to the ERA5 reanalysis data set. There is broad agreement with the albedo patterns. The quasi-uniform grids have low snow fractions in the central-west and north-west coastal regions, and both lat-lon and quasi-uniform grids have anomalously low snow fractions along the southeast and southwestern coasts. In contrast, the `Arctic` grid has larger snow fractions around the south and western coasts, in better agreement with ERA5. The `Arctic` – GrIS grid has low snow fractions along the western coasts, similar to the lat-lon and quasi-uniform grids.

To the extent that the snow fraction changes are responsible for the albedo anomalies in the lat-lon and quasi-uniform grids, we seek to understand the snow cover changes. As the lat-lon and quasi-uniform grids accumulate too much precipitation in the GrIS interior, it is possible that the coastal ice margins—where seasonal melt typically occurs—receive too little snow, which may be more easily melted away to expose the underlying glacial ice. However, Figure 9 does not support a reduction in precipitation along the coastal margins, even when only plotting the solid precipitation (not shown). Instead it seems more likely that the warmer near surface environment, especially in the quasi-uniform grids, leads to anomalously low snow cover and consequent albedo changes.

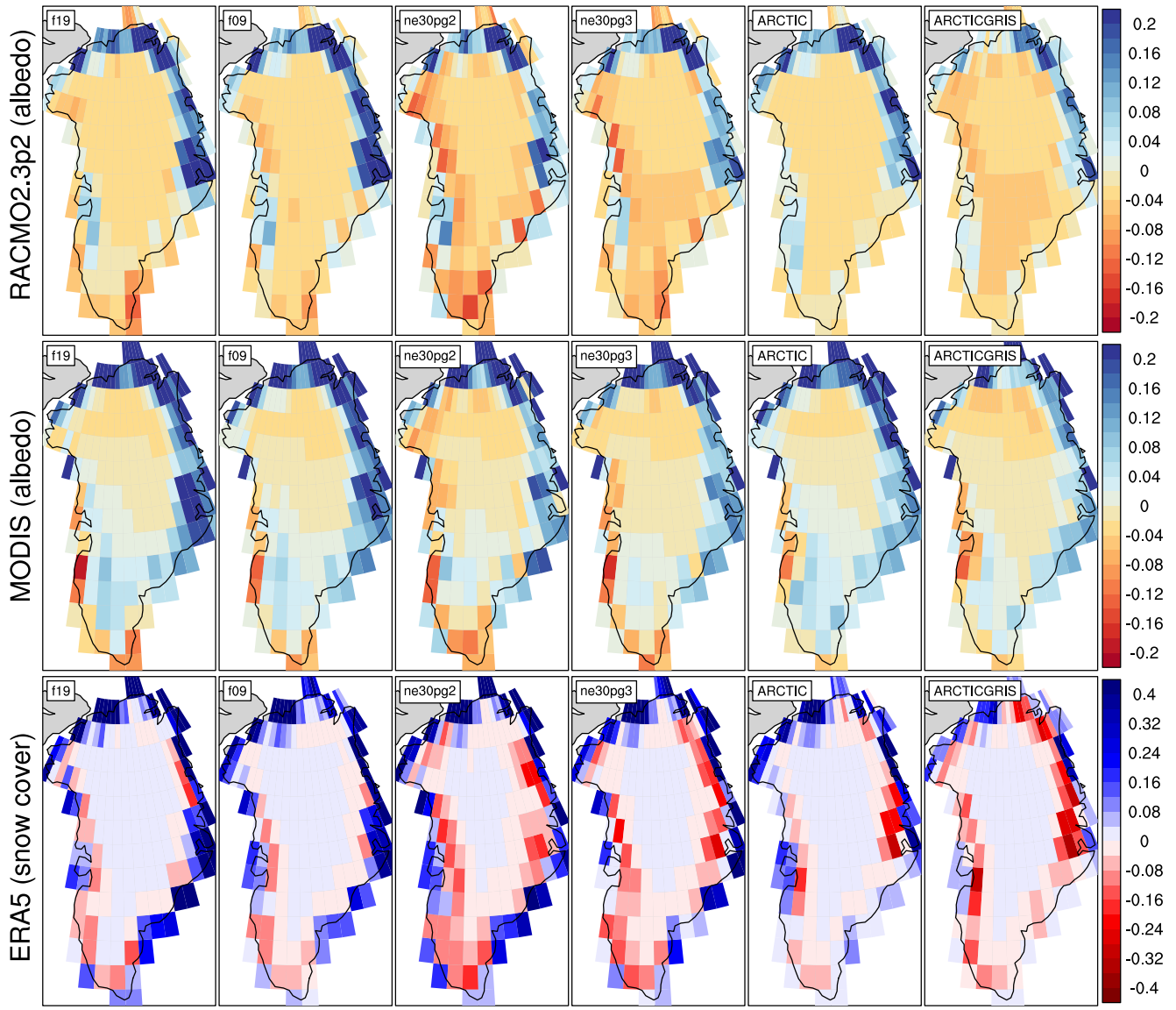

Figure 14. (Middle and bottom) 1979–1998 northern hemisphere summer albedo bias (fraction), computed as the difference (middle) from RACMO2.3p2, and (bottom) the MODIS data set of Tedesco and Alexander (2013). (Bottom) 1979–1998 bias in summer snow cover (fraction) relative to ERA5. All model and validation data have been mapped to the `f19` grid to facilitate the comparison across the different grids.

3.4. Precipitation Extremes

Synoptic storms are tracked using TempestExtremes atmospheric feature detection software (Ullrich et al., 2021). As the `Arctic` grid contains 1/4° refinement north of about 45° latitude, the storm tracker is applied to this region for the `Arctic` and `ne30pg3` runs to identify differences in storm characteristics due to horizontal resolution.

Figure 15 shows monthly PDF (probability density function) of the precipitation rates associated with storms. The PDFs are constructed by sampling all the precipitation rates within 30° of the storm center, for each point on the storm track and for all storms. The PDFs are evaluated on an identical composite grid for all runs, and so storm statistics are not impacted by differences in output resolution. The `Arctic` run has larger extreme precipitation rates compared to `ne30pg3` in every month, but the increase is greatest in the summer months, which coincides with the most extreme events of the year. This is primarily due to increased resolution and not the reduced physics time step; the `ne30pg3`* run only marginally increases the extreme precipitation rates compared with `ne30pg3` (Figure 15).

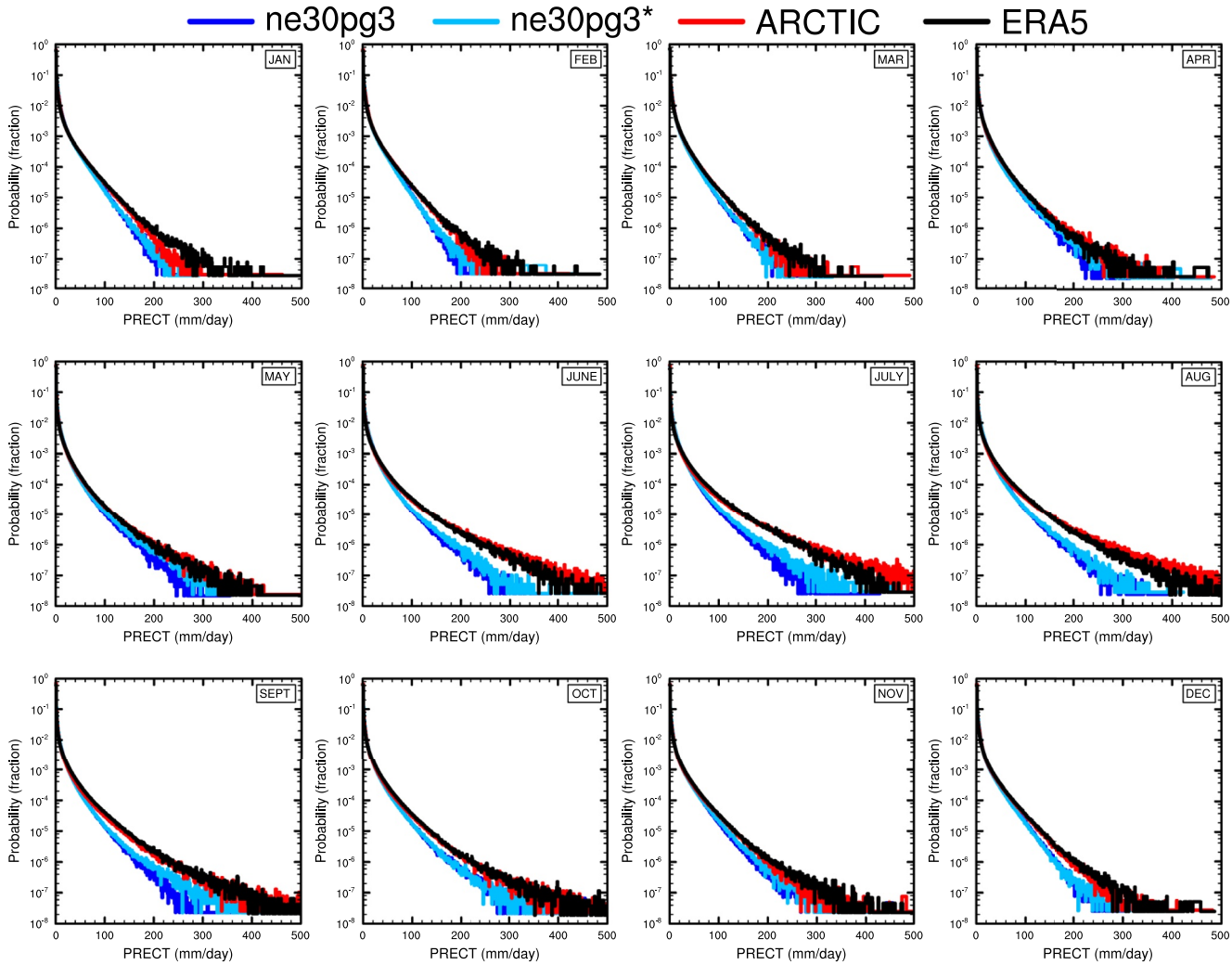

Figure 15. PDFs of the total precipitation rate associated with tracked storms, by month, in the ne30pg3, ne30pg3* and Arctic runs, and compared with the ERA5 data set.

The extreme precipitation rates in the Arctic run are closer than ne30pg3 to the ERA5 reanalysis (Figure 15). It is difficult to know how much the extreme precipitation rates in ERA5 are constrained by data assimilation, or whether these precipitation rates are due to using a similar 1/4° model as the Arctic grid. However, it is well documented that 1/4° models are more skillful at simulating extreme events (Bacmeister et al., 2013; Obrien et al., 2016). A more realistic representation of extreme precipitation events is an additional benefit of the VR grids.

4. Conclusions

Running CESM2.2 in an AMIP style configuration, we have evaluated six grids from two dynamical cores for their performance over the Arctic and in simulating the GrIS SMB. The 1–2° FV grids have enhanced resolution over polar regions due to their convergence of meridian lines, although a polar filter is used to prevent spurious atmospheric features from forming in these regions. SE grids comparable to the resolution of the FV grids have an isotropic grid structure where the grid resolution is similar over the entire model domain. We developed two VR grids and introduced them into CESM2.2 as part of this work. Both use the SE dycore; the Arctic grid has 1/4° refinement over the broader Arctic, whereas the Arctic − GrIS grid is identical except for a 1/8° patch of refinement over Greenland. A third VR grid, CONUS, with 1/8° refinement over the contiguous US, has also been made available in CESM2.2.

In general, the FV grids simulate colder summer temperatures over the Arctic compared with the SE grids (including the VR grids). The cloud biases in all the lat-lon and quasi-uniform resolution grids (FV and SE) are similar, in general being too cloudy over Arctic land masses. It should be emphasized that our analysis is specific

to the Arctic summer because of its relevance to GrIS melt rates. An improved representation of clouds in the Arctic does not imply improved clouds at lower latitudes.

At the regional level, there is a halo of negative cloudiness bias around the ocean perimeter of Greenland on all 1–2° grids, but not the VR grids. This negative cloud bias contrasts with a positive cloud bias over the ice sheet interior. This anomaly pattern is attributed to deficient orographic precipitation in the coarser model grids. With overly smooth topography on the 1–2° grids, synoptic systems moving into Greenland are not sufficiently lifted when encountering the steep ice margins. As a result, excess precipitation falls in the GrIS interior, instead of being concentrated on the steep coastal margins as shown by observations (Pollard & Groups, 2000; Van Kampenhout et al., 2019). This results in a positive precipitation and cloud bias in the ice sheet interior, and a halo of low cloud bias about the perimeter. The agreement of different observational data products on this bias lends confidence in the attribution of causes. The VR grids compare better to the observations and show that orographic precipitation in Greenland is largely resolved when the horizontal resolution is increased sufficiently.

We integrated the primary source and sink terms of the SMB equation over the GrIS for each of the six grids. The 1°–2° lat-lon and quasi-uniform grids have large positive accumulation biases because they fail to resolve orographic precipitation. The quasi-uniform SE grids have larger accumulation biases, suggesting that the FV grids are more skillful for precipitation due to finer resolution over Greenland, and despite a polar filter. The VR grids have the most accurate accumulation rates of all the grids. The primary mass sink term of the GrIS, ice/snow melt, has similar biases; the coarse grids melt too much, with a greater bias for quasi-uniform SE grids. In general, on coarse grids, errors in the individual SMB terms are larger than the errors in the SMB itself, due to compensating errors. This observation serves as a precaution; projecting mass-loss from a glacier or ice sheet cannot be reliable if the processes representing the components of the SMB are incorrect from the start, even if the total SMB has the right magnitude.

The Arctic – GrIS grid has the warmest summer lower troposphere of all grids, yet it has less melting than the quasi-uniform resolution SE grids. This suggests that grid resolution (in coarse grids) is contributing to the melt biases in a way that is not obvious from the large-scale dynamics. The mechanism we propose is that coarse grids represent ablation zones using grid cells with mixed surface types, ice-covered and ice-free. The warmer ice-free patches may largely determine the mean state, leading to a warm bias over the ice-covered patches of the grid cell. This mechanism is supported by analysis of melt biases binned by grid-cell ice fraction. We leave further analysis of this hypothesis to future work.

The Arctic grid substantially improves the simulated Arctic climate, including precipitation extremes and the GrIS SMB, compared to the 1°–2° lat-lon and quasi-uniform grids. The Arctic – GrIS grid has the most realistic cloud and precipitation fields, but the summer temperatures are too warm. The 1° FV model simulates a surprisingly realistic SMB, likely due to the relatively fine resolution of Greenland on lat-lon grids (but perhaps also because it is the most heavily tuned model configuration in CESM). In particular, a greater number of grid cells in the ablation zone reduces the influence of mixed ice-covered/ice-free grid cells that represent ablation poorly on the other (coarser) lat-lon and quasi-uniform grids.

As modeling systems move away from lat-lon grids toward quasi-uniform unstructured grids, it is worth taking stock of whether this will degrade the simulated polar climate. We have found that the 1° FV model has clear advantages over the 1° SE model for simulating the GrIS SMB. The SE dycore is still under active development (e.g., Appendix A) compared to the more mature FV dycore, and future algorithmic improvements may reduce the FV-SE GrIS SMB skill gap. However, such developments are unlikely to eliminate this skill gap entirely, because quasi-uniform unstructured grids have fewer grid cells representing high-latitude structures. Thus, the simulated GrIS SMB will likely be adversely impacted in future CESM versions, after the FV dycore is phased out. This finding will not interrupt the ongoing transition toward unstructured grids in CESM however, which is largely driven by gains in computational efficiency and grid refinement capabilities. We therefore provide the Arctic refined-meshes to the community by way of CESM2.2, providing users the option to simulate a more realistic GrIS SMB, although at a substantial computational premium relative to conventional 1°–2° grids.

We are working to develop a configuration of the Arctic grid that is fully coupled with the CESM ocean and sea ice components and the Community Ice Sheet Model (CISM), to provide multi-century projections of the state of the GrIS and its contribution to sea-level rise. We have also developed a visualization of the Arctic – GrIS run, now available on YouTube (see link in Acknowledgments) to increase awareness of the capabilities of CESM2.2. Figure 16 shows a snapshot of this visualization, illustrating mesoscale katabatic winds descending the south-

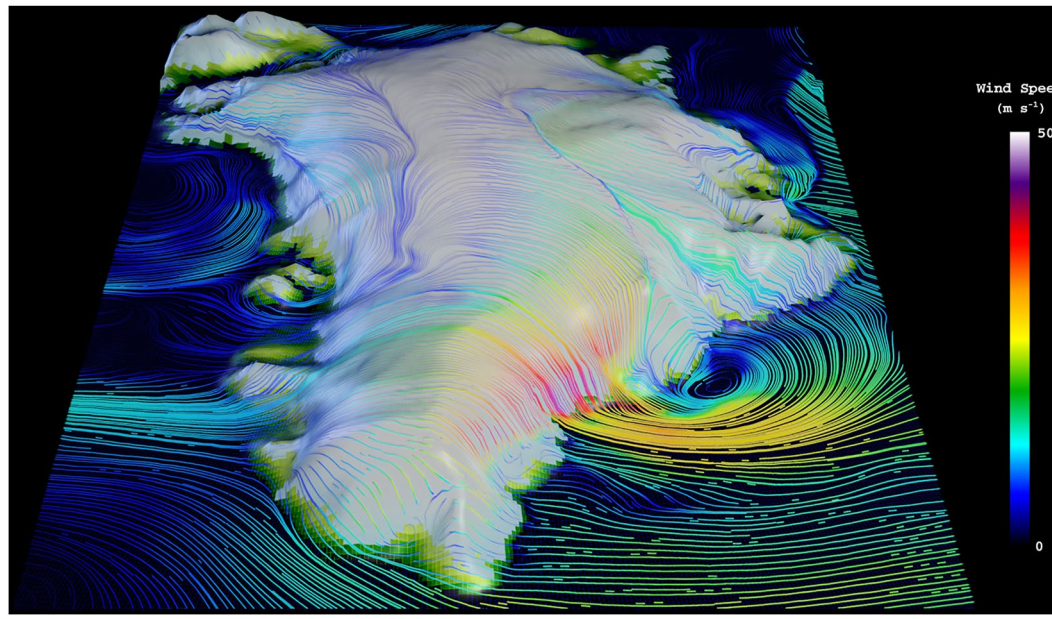

Figure 16. Snapshot of the lowest model level streamlines from the Arctic − GrIS visualization, with color shading denoting the wind magnitude.

eastern slopes of the GrIS. These new grids and configurations will provide new opportunities for CESM polar science, and they aim to contribute to an improved understanding of the polar environment. However, we recognize the potentially prohibitive costs for some users, and so will continue to explore different grids, parameterizations and workflows that can provide some of the same benefits of the VR grids, but at a lower cost.

Appendix A: Details on Spectral-Element Dynamical Core Improvements Since the CESM2.0 Release

Since the CESM2.0 release of the spectral-element dynamical core documented in Lauritzen et al. (2018) some important algorithmic improvements have been implemented and released with CESM2.2. These pertain mainly to the flow over orography that, for the spectral-element dynamical core, can lead to noise aligned with the element boundaries (Herrington et al., 2018).

A1. Reference Profiles

Significant improvement in removing noise for flow over orography can be achieved by using reference profiles for temperature and pressure

$$T^{(\mathrm{ref})} = T_0 + T_1 \Pi^{(\mathrm{ref})}, \tag{A1}$$

$$p_s^{(\mathrm{ref})} = p_0 \exp\left(-\frac{\Phi_s}{R^{(d)} T_{ref}}\right), \tag{A2}$$

(Simmons & Jiabin, 1991) where $T_1 = \Gamma_0 T_{ref} c_p^{(d)}/g \approx 192K$, with gravity g, and standard lapse rate $\Gamma_0 \equiv 6.5$ K/km and $T_0 \equiv T_{ref} - T_1 \approx 97$ K; $T_{ref} = 288$ K ($c_p^{(d)}$ specific heat of dry air at constant pressure; $R^{(d)}$ gas constant for dry air), and Φ_s is the surface geopotential. The reference Exner function is

$$\Pi^{(\mathrm{ref})} = \left(\frac{p^{(\mathrm{ref})}}{p_0}\right)^{\kappa} \tag{A3}$$

where $\kappa = \frac{R^{(d)}}{c_p^{(d)}}$. The reference surface pressure $p_0 = 1{,}000$ hPa and at each model level the reference pressure $p^{(ref)}$ is computed from $p_s^{(\mathrm{ref})}$ and the standard hybrid coefficients

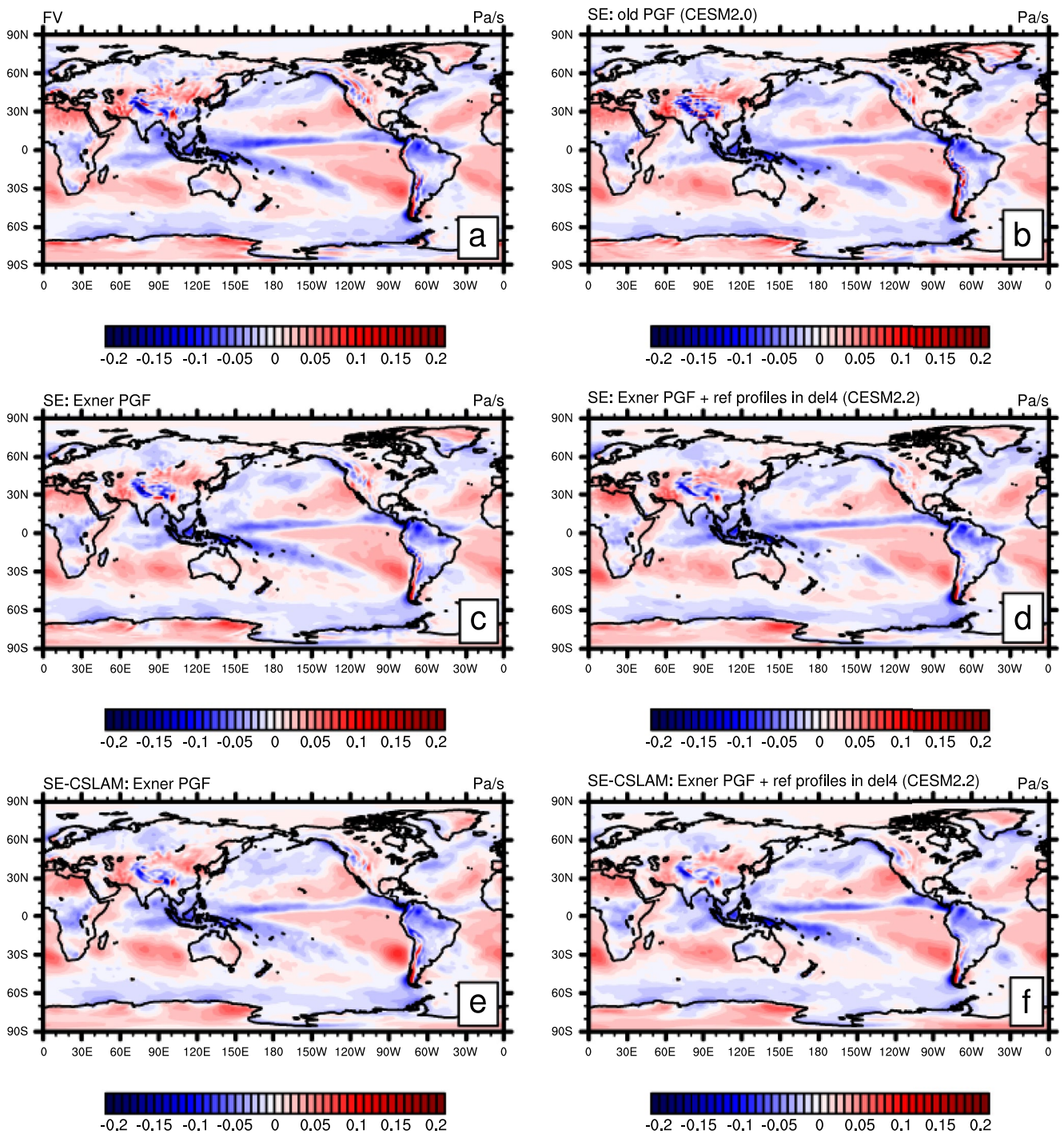

Figure A1. One year averages of vertical pressure velocity at 500 hPa (OMEGA500) using (a) CAM-FV (Finite-Volume dynamical core) and (b–f) various versions of the spectral-element (SE) dynamical core at approximately 1° horizontal resolution and using 32 levels. Plot (b) is equivalent to the CESM2.0 version of the SE dynamical core using the "traditional"/"old" discretization of the pressure-gradient force (PGF). Plot (c) is equivalent to configuration (b) but using the Exner form of the PGF. Plot (d) is the same as configuration (c) but also subtracting reference profiles from pressure and temperature before applying hyperviscosity operators (which is equivalent to the CESM2.2 version of SE in terms of the dynamical core). Plots (e and f) are equivalent to (c and d), respectively, by using the SE-CSLAM (ne30pg3) version of the SE dynamical core (i.e., separate quasi-uniform physics grid and CSLAM transport scheme).

$$p^{(\mathrm{ref})}(\eta) = A(\eta)p_0 + B(\eta)p_s^{(\mathrm{ref})}, \tag{A4}$$

where A and B are the standard hybrid coefficients (using a dry-mass generalized vertical mass coordinate η). These reference profiles are subtracted from the prognostic temperature and pressure-level-thickness states before applying hyperviscosity:

$$\text{CESM2.0} \quad \rightarrow \quad \text{CESM2.2}$$

$$\nabla_\eta^4 T \quad \rightarrow \quad \nabla_\eta^4 \left(T - T^{(\mathrm{ref})}\right), \tag{A5}$$

$$\nabla_\eta^4 \delta p^{(d)} \rightarrow \nabla_\eta^4 \left(\delta p^{(d)} - \delta p^{(\mathrm{ref})}\right). \tag{A6}$$

This reduces spurious transport of temperature and mass up/down-slope due to the hyperviscosity operator.

A2. Rewriting the Pressure Gradient Force (PGF)

In the CESM2.0 the following (standard) form of the pressure gradient term was used:

$$\nabla_\eta \Phi + \frac{1}{\rho}\nabla_\eta p, \tag{A7}$$

where Φ is geopotential and $\rho = \frac{R^{(d)}T_v}{p}$ is density (for details see Lauritzen et al. [2018]). To alleviate noise for flow over orography, we switched to an Exner pressure formulation following Taylor et al. (2020), which uses that Equation A7 can be written in terms of the Exner pressure

$$\nabla_\eta \Phi + c_p^{(d)}\theta_v \nabla_\eta \Pi, \tag{A8}$$

where the Exner pressure is

$$\Pi \equiv \left(\frac{p}{p_0}\right)^\kappa. \tag{A9}$$

and virtual temperature is

$$T_v = T\left(\frac{1 + \frac{1}{\epsilon}m^{(\mathrm{wv})}}{\sum_{\ell \in \mathcal{L}_{all}} m^{(\ell)}}\right), \tag{A10}$$

where $m^{(\ell)}$ is dry mixing ratio of component of moist air ℓ; $\mathcal{L}_{all}$ is the set of all components of moist air and, in particular, "wv" is water vapor.

The derivation showing that Equations A7 and A8 are equivalent is given here:

$$\begin{aligned}
c_p^{(d)}\theta_v \nabla_\eta \Pi &= c_p^{(d)}\theta_v \nabla_\eta \left(\frac{p}{p_0}\right)^\kappa, \\
&= c_p^{(d)}\theta_v \kappa \left(\frac{p}{p_0}\right)^{\kappa-1} \nabla_\eta \left(\frac{p}{p_0}\right), \\
&= c_p^{(d)}\theta_v \kappa \Pi \left(\frac{p_0}{p}\right) \nabla_\eta \left(\frac{p}{p_0}\right), \\
&= \frac{c_p^{(d)}\theta_v \kappa \Pi}{p} \nabla_\eta p, \\
&= \frac{R^{(d)}\theta_v \Pi}{p} \nabla_\eta p, \\
&= \frac{R^{(d)}T_v}{p} \nabla_\eta p, \\
&= \frac{1}{\rho}\nabla_\eta p.
\end{aligned}$$

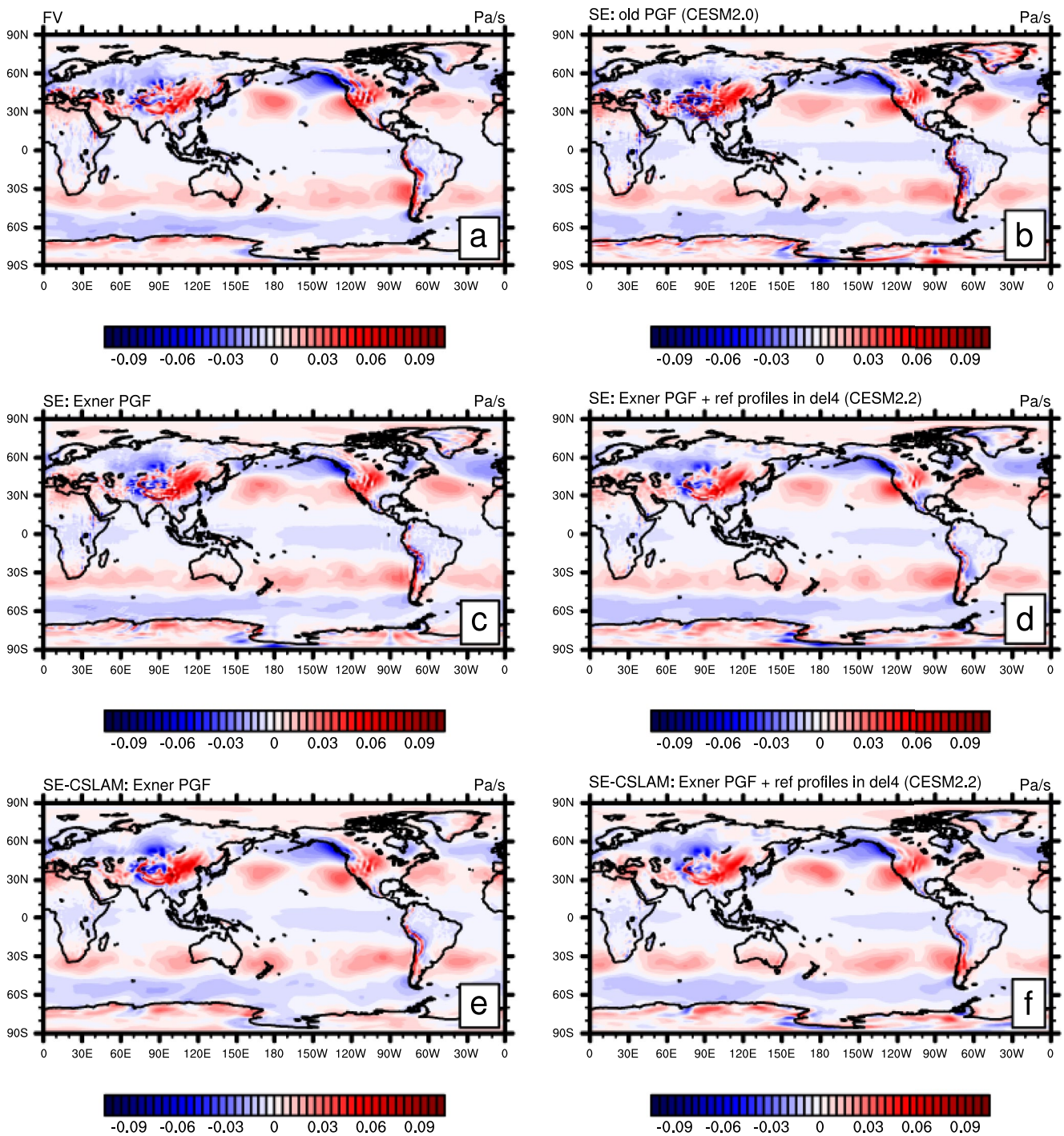

Figure A2. Same as Figure A1 but using modified Held-Suarez forcing and the average is over 18 months (excl. spin-up).

where virtual potential temperature is T_v/Π. Using the reference states from Simmons and Jiabin (1991),

$$\overline{T} = T_0 + T_1\Pi, \tag{A11}$$

$$\overline{\theta} = T_0/\Pi + T_1, \tag{A12}$$

we can define a geopotential as a function of Exner pressure

$$\overline{\Phi} = -c_p^{(d)}\left(T_0 \log\Pi + T_1\Pi - T_1\right). \tag{A13}$$

This "balanced" geopotential obeys

$$c_p^{(d)}\overline{\theta}\nabla\Pi + \nabla\overline{\Phi} = 0 \tag{A14}$$

for any Exner pressure. Subtracting this "reference" profile from the PGF yields

$$\begin{aligned} \nabla_\eta\Phi + c_p^{(d)}\theta_v\nabla_\eta\Pi &= \nabla_\eta\left(\Phi - \overline{\Phi}\right) + c_p^{(d)}\left(\theta_v - \overline{\theta}\right)\nabla_\eta\Pi, \\ &= \nabla_\eta\Phi + c_p^{(d)}\theta_v\nabla_\eta\Pi + c_p^{(d)}T_0\left[\nabla_\eta\log\Pi - \frac{1}{\Pi}\nabla_\eta\Pi\right]. \end{aligned} \tag{A15}$$

In the continuum, the two formulations (left and right-hand side of Equation A15) are identical. But under discretization, the second formulation can have much less truncation error.

A3. Results

One year averages of vertical pressure velocity at 500 hPa (OMEGA500) have been found to be a useful quantity to detect spurious up or down-drafts induced by steep orography (Figure A1). While the true solution is not known, strong vertical velocities aligned with element edges that are not found in the CAM-FV reference solution (Figure A1a) are likely not physical (spurious). The older CESM2.0 version of SE (Figure A1d) using the "traditional" discretization of the PGF, (A15), exhibits significant spurious noise patters around steep orography compared to CAM-FV (e.g., around Himalayas and Andes). This is strongly alleviated by switching to the Exner formulation of the PGF (A8; Figure A1c). By also subtracting reference profiles from pressure-level thickness and temperature, Equation A5 and A6 respectively, reduces strong up-down drafts further (Figure A1d). Switching to the CAM-SE-CSLAM version where physics tendencies are computed on an quasi-equal area physics grid and using the CSLAM transport scheme, marginal improvements are observed in terms of a smoother vertical velocity field (Figures A1e and A1f). The configuration shown in Figure A1d is used for the simulations shown in the main text of this paper.

It is interesting to note that the noise issues and algorithmic remedies found in the real-world simulations discussed above, can be investigated by replacing all of physics with a modified version of the Held-Suarez forcing (Held & Suarez, 1994). The original formulation of the Held-Suarez idealized test case used a flat Earth ($\Phi_s = 0$) and a dry atmosphere. By simply adding the surface topography used in "real-world" simulations and removing the temperature relaxation in the lower part of domain ($\sigma > 0.7$; see Held and Suarez [1994] for details), surprisingly realistic vertical velocity fields (in terms of structure) result (see Figure A2). Since this was a very useful development tool it is shared in this manuscript.

Data Availability Statement

The data presented in main part of this manuscript is available at https://github.com/adamrher/2020-arcticgrids. The source code and data for the Appendix is available at https://github.com/PeterHjortLauritzen/CAM/tree/topo-mods.

Acknowledgments
This material is based upon work supported by the National Center for Atmospheric Research (NCAR), which is a major facility sponsored by the NSF under Cooperative Agreement 1852977. Computing and data storage resources, including the Cheyenne supercomputer (Computational and Information Systems Laboratory, 2017), were provided by the Computational and Information Systems Laboratory (CISL) at NCAR. A. Herrington was funded through the NCAR Advanced Study Program Postdoctoral Fellowship. A. Herrington thanks Matt Rehme (NCAR/CISL) for his role in generating the Arctic − GrIS visualization available on youtube (https://www.youtube.com/watch?v=YwHgqDu75s8&t=4s&abchannel=NCAR-VisLab). To download CESM2.2, go to https://github.com/ESCOMP/CESM and check-out the latest $\tt cesm2_2$ tag.

References

Alexander, P., LeGrande, A., Fischer, E., Tedesco, M., Fettweis, X., Kelley, M., et al. (2019). Simulated Greenland surface mass balance in the GISS ModelE2 GCM: Role of the ice sheet surface. *Journal of Geophysical Research: Earth Surface*, *124*(3), 750–765. https://doi.org/10.1029/2018jf004772

Bacmeister, J. T., Reed, K. A., Hannay, C., Lawrence, P., Bates, S., Truesdale, J. E., et al. (2016). Projected changes in tropical cyclone activity under future warming scenarios using a high-resolution climate model. *Climatic Change*, *146*(3–4), 547–560. https://doi.org/10.1007/s10584-016-1750-x

Bacmeister, J. T., Wehner, M. F., Neale, R. B., Gettelman, A., Hannay, C., Lauritzen, P. H., et al. (2013). Exploratory high-resolution climate simulations using the Community Atmosphere Model (CAM). *Journal of Climate*, *27*(9), 3073–3099. https://doi.org/10.1175/JCLI-D-13-00387.1

Bambach, N. E., Rhoades, A. M., Hatchett, B. J., Jones, A. D., Ullrich, P. A., & Zarzycki, C. M. (2021). Projecting climate change in South America using variable-resolution Community Earth System Model: An application to Chile. *International Journal of Climatology*, *42*(4), 2514–2542. https://doi.org/10.1002/joc.7379

Beljaars, A., Brown, A., & Wood, N. (2004). A new parametrization of turbulent orographic form drag. *Quarterly Journal of the Royal Meteorological Society*, *130*(599), 1327–1347. https://doi.org/10.1256/qj.03.73

Bogenschutz, P. A., Gettelman, A., Morrison, H., Larson, V. E., Craig, C., & Schanen, D. P. (2013). Higher-order turbulence closure and its impact on climate simulations in the community atmosphere model. *Journal of Climate*, *26*(23), 9655–9676. https://doi.org/10.1175/jcli-d-13-00075.1

Box, J. E., Bromwich, D. H., & Bai, L.-S. (2004). Greenland ice sheet surface mass balance 1991–2000: Application of Polar MM5 mesoscale model and in situ data. *Journal of Geophysical Research*, *109*(D16), D16105. https://doi.org/10.1029/2003jd004451

Braithwaite, R. J. (1984). Calculation of degree-days for glacier-climate research. *Zeitschrift für Gletscherkunde und Glazialgeologie*, *20*, 1–8.

Burakowski, E. A., Tawfik, A., Ouimette, A., Lepine, L., Zarzycki, C., Novick, K., et al. (2019). Simulating surface energy fluxes using the variable-resolution Community Earth System Model (VR-CESM). *Theoretical and Applied Climatology*, *138*(1), 115–133. https://doi.org/10.1007/s00704-019-02785-0

Calov, R., & Greve, R. (2005). A semi-analytical solution for the positive degree-day model with stochastic temperature variations. *Journal of Glaciology*, *51*(172), 173–175. https://doi.org/10.3189/172756505781829601

Canuto, C., Hussaini, M. Y., Quarteroni, A., & Zang, T. (2007). *Spectral methods: Evolution to complex geometries and applications to fluid dynamics* (1st ed.). Springer.

Chang, P., Zhang, S., Danabasoglu, G., Yeager, S. G., Fu, H., Wang, H., et al. (2020). An unprecedented set of high-resolution Earth system simulations for understanding multiscale interactions in climate variability and change. *Journal of Advances in Modeling Earth Systems*, *12*(12), e2020MS002298. https://doi.org/10.1029/2020ms002298

Chepfer, H., Bony, S., Winker, D., Cesana, G., Dufresne, J., Minnis, P., et al. (2010). The GCM-oriented CALIPSO cloud product (CALIPSO-GOCCP). *Journal of Geophysical Researc*h, *115*(D4), D00H16. https://doi.org/10.1029/2009jd012251

Collins, W. D., Rasch, P. J., Boville, B. A., Hack, J. J., McCaa, J. R., Williamson, D. L., et al. (2006). The formulation and atmospheric simulation of the Community Atmosphere Model version 3 (CAM3). *Journal of Climate*, *19*(11), 2144–2161. https://doi.org/10.1175/jcli3760.1

Computational and Information Systems Laboratory. (2017). *Cheyenne: HPE/SGI ICE XA system (Climate Simulation Laboratory)*. National Center for Atmospheric Research. https://doi.org/10.5065/D6RX99HX

Copernicus, C. (2019). ERA5 monthly averaged data on pressure levels from 1979 to present. Retrieved from https://cds.climate.copernicus.eu

Craig, C., Bacmeister, J., Callaghan, P., Eaton, B., Gettelman, A., Goldhaber, S. N., et al. (2021). *CAM6.3 user's guide* (Technical Report). NCAR/TN-571+EDD. https://doi.org/10.5065/Z953-ZC95

Danabasoglu, G., Lamarque, J.-F., Bacmeister, J., Bailey, D., DuVivier, A., Edwards, J., et al. (2020). The Community Earth System Model version 2 (CESM2). *Journal of Advances in Modeling Earth Systems*, *12*(2), e2019MS001916. https://doi.org/10.1029/2019MS001916

Danielson, J., & Gesch, D. (2011). *Global multi-resolution terrain elevation data 2010 (GMTED2010) (Open-File Report 2011-1073)*. U.S. Geological Survey. Retrieved from http://pubs.usgs.gov/of/2011/1073/pdf/of2011-1073.pdf

Dennis, J., Edwards, J., Evans, K. J., Guba, O., Lauritzen, P. H., Mirin, A. A., et al. (2012). CAM-SE: A scalable spectral element dynamical core for the Community Atmosphere Model. *International Journal of High Performance Computing Applications*, *26*(1), 74–89. https://doi.org/10.1177/1094342011428142

Dennis, J., Fournier, A., Spotz, W., St-Cyr, A., Taylor, M., Thomas, S., & Tufo, H. (2005). High-resolution mesh convergence properties and parallel efficiency of a spectral element atmospheric dynamical core. *International Journal of High Performance Computing Applications*, *19*(3), 225–235. https://doi.org/10.1177/1094342005056108

Evans, K. J., Kennedy, J. H., Lu, D., Forrester, M. M., Price, S., Fyke, J., et al. (2019). LIVVkit 2.1: Automated and extensible ice sheet model validation. *Geoscientific Model Development*, *12*(3), 1067–1086. https://doi.org/10.5194/gmd-12-1067-2019

Eyring, V., Bony, S., Meehl, G. A., Senior, C. A., Stevens, B., Stouffer, R. J., & Taylor, K. E. (2016). Overview of the Coupled Model Intercomparison Project Phase 6 (CMIP6) experimental design and organization. *Geoscientific Model Development*, *9*(5), 1937–1958. https://doi.org/10.5194/gmd-9-1937-2016

Fettweis, X., Franco, B., Tedesco, M., Van Angelen, J., Lenaerts, J. T., van den Broeke, M. R., & Gallée, H. (2013). Estimating the Greenland ice sheet surface mass balance contribution to future sea level rise using the regional atmospheric climate model MAR. *The Cryosphere*, *7*(2), 469–489. https://doi.org/10.5194/tc-7-469-2013

Fyke, J. G., Sergienko, O., Lofverstrom, M., Price, S., & Lenaerts, J. T. (2018). An overview of interactions and feedbacks between ice sheets and the Earth system. *Reviews of Geophysics*, *56*(2), 361–408. https://doi.org/10.1029/2018RG000600

Gettelman, A., Callaghan, P., Larson, V., Zarzycki, C., Bacmeister, J., Lauritzen, P., et al. (2017). Regional climate simulations with the community Earth system model. *Journal of Advances in Modeling Earth Systems*, *10*(6), 1245–1265. https://doi.org/10.1002/2017ms001227

Gettelman, A., Hannay, C., Bacmeister, J. T., Neale, R. B., Pendergrass, A., Danabasoglu, G., et al. (2019). High climate sensitivity in the Community Earth System Model version 2 (CESM2). *Geophysical Research Letters*, *46*(14), 8329–8337. https://doi.org/10.1029/2019gl083978

Gettelman, A., & Morrison, H. (2015). Advanced two-moment bulk microphysics for global models. Part I: Off-line tests and comparison with other schemes. *Journal of Climate*, *28*(3), 1268–1287. https://doi.org/10.1175/jcli-d-14-00102.1

Gettelman, A., Morrison, H., Santos, S., Bogenschutz, P., & Caldwell, P. (2015). Advanced two-moment bulk microphysics for global models. Part II: Global model solutions and aerosol–cloud interactions. *Journal of Climate*, *28*(3), 1288–1307. https://doi.org/10.1175/jcli-d-14-00103.1

Golaz, J.-C., Larson, V. E., & Cotton, W. R. (2002). A PDF-based model for boundary layer clouds. Part I: Method and model description. *Journal of the Atmospheric Sciences*, *59*(24), 3540–3551. https://doi.org/10.1175/1520-0469(2002)059<3540:apbmfb>2.0.co;2

Guba, O., Taylor, M. A., Ullrich, P. A., Overfelt, J. R., & Levy, M. N. (2014). The spectral element method (SEM) on variable-resolution grids: Evaluating grid sensitivity and resolution-aware numerical viscosity. *Geoscientific Model Development*, *7*(6), 2803–2816. https://doi.org/10.5194/gmd-7-2803-2014

Guo, Z., Wang, M., Qian, Y., Larson, V. E., Ghan, S., Ovchinnikov, M., et al. (2015). Parametric behaviors of CLUBB in simulations of low clouds in the Community Atmosphere Model (CAM). *Journal of Advances in Modeling Earth Systems*, *7*(3), 1005–1025. https://doi.org/10.1002/2014ms000405

Hansen, N., Simonsen, S. B., Boberg, F., Kittel, C., Orr, A., Souverijns, N., et al. (2022). Brief communication: Impact of common ice mask in surface mass balance estimates over the Antarctic ice sheet. *The Cryosphere*, *16*(2), 711–718. https://doi.org/10.5194/tc-16-711-2022

Held, I. M., & Suarez, M. J. (1994). A proposal for the intercomparison of the dynamical cores of atmospheric general circulation models. *Bulletin of the American Meteorological Society*, *73*(10), 1825–1830. https://doi.org/10.1175/1520-0477(1994)075<1825:apftio>2.0.co;2

Herrington, A. R., Lauritzen, P., Taylor, M. A., Goldhaber, S., Eaton, B. E., Bacmeister, J., et al. (2018). Physics-dynamics coupling with element-based high-order Galerkin methods: Quasi equal-area physics grid. *Monthly Weather Review*, *47*(1), 69–84. https://doi.org/10.1175/MWR-D-18-0136.1

Herrington, A. R., Lauritzen, P. H., Reed, K. A., Goldhaber, S., & Eaton, B. E. (2019). Exploring a lower resolution physics grid in CAM-SE-CSLAM. *Journal of Advances in Modeling Earth Systems*, *11*(7), 1894–1916. https://doi.org/10.1029/2019ms001684

Herrington, A. R., & Reed, K. A. (2018). An idealized test of the response of the community atmosphere model to near-grid-scale forcing across hydrostatic resolutions. *Journal of Advances in Modeling Earth Systems*, *10*(2), 560–575. https://doi.org/10.1002/2017ms001078

Herrington, A. R., & Reed, K. A. (2020). On resolution sensitivity in the community atmosphere model. *Quarterly Journal of the Royal Meteorological Society*, *146*(733), 3789–3807. https://doi.org/10.1002/qj.3873

Hurrell, J. W., Hack, J. J., Shea, D., Caron, J. M., & Rosinski, J. (2008). A new sea surface temperature and sea ice boundary dataset for the community atmosphere model. *Journal of Climate*, *21*(19), 5145–5153. https://doi.org/10.1175/2008jcli2292.1

Jablonowski, C., & Williamson, D. L. (2011). The pros and cons of diffusion, filters and fixers in atmospheric general circulation models. In P. H. Lauritzen, C. Jablonowski, M. Taylor, & R. Nair (Eds.), *Numerical techniques for global atmospheric models* (pp. 381–493). Springer Berlin Heidelberg. https://doi.org/10.1007/978-3-642-11640-7_13

Lauritzen, P. H., Bacmeister, J. T., Callaghan, P. F., & Taylor, M. A. (2015). NCAR_Topo (v1.0): NCAR global model topography generation software for unstructured grids. *Geoscientific Model Development*, *8*(12), 3975–3986. https://doi.org/10.5194/gmd-8-3975-2015

Lauritzen, P. H., Jablonowski, C., Taylor, M., & Nair, R. D. (2010). Rotated versions of the Jablonowski steady-state and baroclinic wave test cases: A dynamical core intercomparison. *Journal of Advances in Modeling Earth Systems*, *2*(15), 34. https://doi.org/10.3894/james.2010.2.15

Lauritzen, P. H., Mirin, A., Truesdale, J., Raeder, K., Anderson, J., Bacmeister, J., & Neale, R. B. (2011). Implementation of new diffusion/filtering operators in the CAM-FV dynamical core. *International Journal of High Performance Computing Applications*, *26*(1), 63–73. https://doi.org/10.1177/1094342011410088

Lauritzen, P. H., Nair, R., Herrington, A., Callaghan, P., Goldhaber, S., Dennis, J., et al. (2018). NCAR release of CAM-SE in CESM2.0: A reformulation of the spectral-element dynamical core in dry-mass vertical coordinates with comprehensive treatment of condensates and energy. *Journal of Advances in Modeling Earth Systems*, *10*(7), 1537–1570. https://doi.org/10.1029/2017MS001257

Lauritzen, P. H., Taylor, M. A., Overfelt, J., Ullrich, P. A., Nair, R. D., Goldhaber, S., & Kelly, R. (2017). CAM-SE-CSLAM: Consistent coupling of a conservative semi-Lagrangian finite-volume method with spectral element dynamics. *Monthly Weather Review*, *145*(3), 833–855. https://doi.org/10.1175/MWR-D-16-0258.1

Lawrence, D. M., Fisher, R. A., Koven, C. D., Oleson, K. W., Swenson, S. C., Bonan, G., et al. (2019). The Community Land Model version 5: Description of new features, benchmarking, and impact of forcing uncertainty. *Journal of Advances in Modeling Earth Systems*, *11*(12), 4245–4287. https://doi.org/10.1029/2018ms001583

Lin, S.-J. (2004). A "vertically Lagrangian" finite-volume dynamical core for global models. *Monthly Weather Review*, *132*(10), 2293–2307. https://doi.org/10.1175/1520-0493(2004)132<2293:avlfdc>2.0.co;2

Lin, S.-J., & Rood, R. B. (1997). An explicit flux-form semi-Lagrangian shallow-water model on the sphere. *Quarterly Journal of the Royal Meteorological Society*, *123*(544), 2477–2498. https://doi.org/10.1002/qj.49712354416

Lipscomb, W. H., Fyke, J. G., Vizcaíno, M., Sacks, W. J., Wolfe, J., Vertenstein, M., et al. (2013). Implementation and initial evaluation of the glimmer community ice sheet model in the Community Earth System Model. *Journal of Climate*, *26*(19), 7352–7371. https://doi.org/10.1175/jcli-d-12-00557.1

Loeb, N. G., Doelling, D. R., Wang, H., Su, W., Nguyen, C., Corbett, J. G., et al. (2018). Clouds and the Earth's radiant energy system (CERES) energy balanced and filled (EBAF) top-of-atmosphere (TOA) edition-4.0 data product. *Journal of Climate*, *31*(2), 895–918. https://doi.org/10.1175/jcli-d-17-0208.1

Lofverstrom, M., Fyke, J. G., Thayer-Calder, K., Muntjewerf, L., Vizcaino, M., Sacks, W. J., et al. (2020). An efficient ice sheet/Earth system model spin-up procedure for CESM2-CISM2: Description, evaluation, and broader applicability. *Journal of Advances in Modeling Earth Systems*, *12*(8), e2019MS001984. https://doi.org/10.1029/2019ms001984

Morlighem, M., Rignot, E., Mouginot, J., Seroussi, H., & Larour, E. (2014). Deeply incised submarine glacial valleys beneath the Greenland ice sheet. *Nature Geoscience*, *7*(6), 418–422. https://doi.org/10.1038/ngeo2167

Mottram, R., Boberg, F., Langen, P., Yang, S., Rodehacke, C., Christensen, J. H., & Madsen, M. S. (2017). Surface mass balance of the Greenland ice sheet in the regional climate model HIRHAM5: Present state and future prospects. *Low Temperature Science*, *75*, 105–115.

Muntjewerf, L., Sacks, W. J., Lofverstrom, M., Fyke, J., Lipscomb, W. H., Ernani da Silva, C., et al. (2021). Description and demonstration of the coupled Community Earth System Model v2–Community Ice Sheet Model v2 (CESM2-CISM2). *Journal of Advances in Modeling Earth Systems*, *13*(6), e2020MS002356. https://doi.org/10.1029/2020ms002356

Neale, R. B., Richter, J. H., & Jochum, M. (2008). The impact of convection on ENSO: From a delayed oscillator to a series of events. *Journal of Climate*, *21*(22), 5904–5924. https://doi.org/10.1175/2008jcli2244.1

Noël, B., van de Berg, W. J., Lhermitte, S., & van den Broeke, M. R. (2019). Rapid ablation zone expansion amplifies north Greenland mass loss. *Science Advances*, *5*(9), eaaw0123. https://doi.org/10.1126/sciadv.aaw0123

Noël, B., van de Berg, W. J., Van Meijgaard, E., Kuipers Munneke, P., Van De Wal, R., & Van Den Broeke, M. (2015). Evaluation of the updated regional climate model RACMO2. 3: Summer snowfall impact on the Greenland Ice Sheet. *The Cryosphere*, *9*(5), 1831–1844. https://doi.org/10.5194/tc-9-1831-2015

Noël, B., van de Berg, W. J., Van Wessem, J. M., Van Meijgaard, E., Van As, D., Lenaerts, J., et al. (2018). Modelling the climate and surface mass balance of polar ice sheets using RACMO2–Part 1: Greenland (1958–2016). *The Cryosphere*, *12*(3), 811–831. https://doi.org/10.5194/tc-12-811-2018

Obrien, T. A., Collins, W. D., Kashinath, K., Rübel, O., Byna, S., Gu, J., et al. (2016). Resolution dependence of precipitation statistical fidelity in hindcast simulations. *Journal of Advances in Modeling Earth Systems*, *8*(2), 976–990. https://doi.org/10.1002/2016ms000671

Ohmura, A. (2001). Physical basis for the temperature-based melt-index method. *Journal of Applied Meteorology*, *40*(4), 753–761. https://doi.org/10.1175/1520-0450(2001)040<0753:pbfttb>2.0.co;2

Pfister, G. G., Eastham, S. D., Arellano, A. F., Aumont, B., Barsanti, K. C., Barth, M. C., et al. (2020). The multi-scale infrastructure for chemistry and aerosols (MUSICA). *Bulletin of the American Meteorological Society*, *101*(10), E1743–E1760. https://doi.org/10.1175/bams-d-19-0331.1

Pollard, D. (2010). A retrospective look at coupled ice sheet–climate modeling. *Climatic Change*, *100*(1), 173–194. https://doi.org/10.1007/s10584-010-9830-9

Pollard, D., & Groups, P. P. (2000). Comparisons of ice-sheet surface mass budgets from paleoclimate modeling intercomparison project (PMIP) simulations. *Global and Planetary Change*, *24*(2), 79–106. https://doi.org/10.1016/s0921-8181(99)00071-5

Pope, V., & Stratton, R. (2002). The processes governing horizontal resolution sensitivity in a climate model. *Climate Dynamics*, *19*(3–4), 211–236. https://doi.org/10.1007/s00382-001-0222-8

Putman, W. M., & Lin, S.-J. (2007). Finite-volume transport on various cubed-sphere grids. *Journal of Computational Physics*, *227*(1), 55–78. https://doi.org/10.1016/j.jcp.2007.07.022

Rae, J., Adalgeirsdóttir, G., Edwards, T. L., Fettweis, X., Gregory, J., Hewitt, H., et al. (2012). Greenland ice sheet surface mass balance: Evaluating simulations and making projections with regional climate models. *The Cryosphere*, *6*(6), 1275–1294. https://doi.org/10.5194/tc-6-1275-2012

Rasch, P. J., & Williamson, D. L. (1990). Computational aspects of moisture transport in global models of the atmosphere. *Quarterly Journal of the Royal Meteorological Society*, *116*(495), 1071–1090. https://doi.org/10.1002/qj.49711649504

Reeh, N. (1991). Parameterization of melt rate and surface temperature in the Greenland ice sheet. *Polarforschung*, *59*(3), 113–128.

Rhoades, A. M., Huang, X., Ullrich, P. A., & Zarzycki, C. M. (2016). Characterizing Sierra Nevada snowpack using variable-resolution CESM. *Journal of Applied Meteorology and Climatology*, *55*(1), 173–196. https://doi.org/10.1175/JAMC-D-15-0156.1

Richter, J. H., Sassi, F., & Garcia, R. R. (2010). Toward a physically based gravity wave source parameterization in a general circulation model. *Journal of the Atmospheric Sciences*, *67*(1), 136–156. https://doi.org/10.1175/2009JAS3112.1

Rignot, E., & Mouginot, J. (2012). Ice flow in Greenland for the international polar year 2008–2009. *Geophysical Research Letters*, *39*(11), L11501. https://doi.org/10.1029/2012gl051634

Roeckner, E., Brokopf, R., Esch, M., Giorgetta, M., Hagemann, S., Kornblueh, L., et al. (2006). Sensitivity of simulated climate to horizontal and vertical resolution in the ECHAM5 atmosphere model. *Journal of Climate*, *19*(16), 3771–3791.

Sellevold, R., Van Kampenhout, L., Lenaerts, J., Noël, B., Lipscomb, W. H., & Vizcaino, M. (2019). Surface mass balance downscaling through elevation classes in an Earth system model: Application to the Greenland ice sheet. *The Cryosphere*, *13*(12), 3193–3208. https://doi.org/10.5194/tc-13-3193-2019

Serreze, M. C., Barrett, A. P., Slater, A. G., Steele, M., Zhang, J., & Trenberth, K. E. (2007). The large-scale energy budget of the Arctic. *Journal of Geophysical Research*, *112*(D11), D11122. https://doi.org/10.1029/2006jd008230

Simmons, A. J., & Jiabin, C. (1991). The calculation of geopotential and the pressure gradient in the ECMWF atmospheric model: Influence on the simulation of the polar atmosphere and on temperature analyses. *Quarterly Journal of the Royal Meteorological Society*, *117*(497), 29–58. https://doi.org/10.1002/qj.49711749703

Small, R. J., Bacmeister, J., Bailey, D., Baker, A., Bishop, S., Bryan, F., et al. (2014). A new synoptic scale resolving global climate simulation using the Community Earth System Model. *Journal of Advances in Modeling Earth Systems*, *6*(4), 1065–1094. https://doi.org/10.1002/2014MS000363

Suarez, M. J., & Takacs, L. L. (1995). Volume 5 documentation of the ARIES/GEOS dynamical core: Version 2.

Taylor, M. A., & Fournier, A. (2010). A compatible and conservative spectral element method on unstructured grids. *Journal of Computational Physics*, *229*(17), 5879–5895. https://doi.org/10.1016/j.jcp.2010.04.008

Taylor, M. A., Guba, O., Steyer, A., Ullrich, P. A., Hall, D. M., & Eldred, C. (2020). An energy consistent discretization of the nonhydrostatic equations in primitive variables. *Journal of Advances in Modeling Earth Systems*, *12*(1). https://doi.org/10.1029/2019MS001783

Taylor, M. A., Tribbia, J., & Iskandarani, M. (1997). The spectral element method for the shallow water equations on the sphere. *Journal of Computational Physics*, *130*(1), 92–108. https://doi.org/10.1006/jcph.1996.5554

Team, E. J. S., Balaji, V., Boville, B., Collins, N., Craig, T., Cruz, C., et al. (2021). ESMF user guide (Technical Report).

Tedesco, M., & Alexander, P. (2013). MODIS (MOD10A1) albedo data on the MAR RCM grid (2000–2013). Retrieved from https://cds.climate.copernicus.eu

Ullrich, P. A., & Taylor, M. A. (2015). Arbitrary-order conservative and consistent remapping and a theory of linear maps: Part I. *Monthly Weather Review*, *143*(6), 2419–2440. https://doi.org/10.1175/mwr-d-14-00343.1

Ullrich, P. A., Zarzycki, C. M., McClenny, E. E., Pinheiro, M. C., Stansfield, A. M., & Reed, K. A. (2021). TempestExtremes v2. 1: A community framework for feature detection, tracking and analysis in large datasets. *Geoscientific Model Development Discussions*, *1–37*(8), 5023–5048. https://doi.org/10.5194/gmd-14-5023-2021

van Kampenhout, L., Lenaerts, J. T., Lipscomb, W. H., Lhermitte, S., Noël, B., Vizcaíno, M., et al. (2020). Present-day Greenland Ice Sheet climate and surface mass balance in CESM2. *Journal of Geophysical Research: Earth Surface*, *125*(2). https://doi.org/10.1029/2019jf005318

Van Angelen, J., Lenaerts, J., Lhermitte, S., Fettweis, X., Kuipers Munneke, P., Van den Broeke, M., et al. (2012). Sensitivity of Greenland Ice Sheet surface mass balance to surface albedo parameterization: A study with a regional climate model. *The Cryosphere*, *6*(5), 1175–1186. https://doi.org/10.5194/tc-6-1175-2012

Van Kampenhout, L., Rhoades, A. M., Herrington, A. R., Zarzycki, C. M., Lenaerts, J., Sacks, W. J., & Van Den Broeke, M. R. (2019). Regional grid refinement in an Earth system model: Impacts on the simulated Greenland surface mass balance. *The Cryosphere*, *13*(6), 1547–1564. https://doi.org/10.5194/tc-13-1547-2019

Wan, H., Giorgetta, M. A., Zängl, G., Restelli, M., Majewski, D., Bonaventura, L., et al. (2013). The ICON-1.2 hydrostatic atmospheric dynamical core on triangular grids—Part I: Formulation and performance of the baseline version. *Geoscientific Model Development*, *6*(3), 735–763. https://doi.org/10.5194/gmd-6-735-2013

Williamson, D. (2007). The evolution of dynamical cores for global atmospheric models. *Journal of the Meteorological Society of Japan*, *85*, 241–269. https://doi.org/10.2151/jmsj.85b.241

Williamson, D. (2008). Convergence of aqua-planet simulations with increasing resolution in the community atmospheric model, version 3. *Tellus A*, *60*(5), 848–862. https://doi.org/10.1111/j.1600-0870.2008.00339.x

Zarzycki, C. M., Jablonowski, C., & Taylor, M. A. (2014). Using variable-resolution meshes to model tropical cyclones in the community atmosphere model. *Monthly Weather Review*, *142*(3), 1221–1239. https://doi.org/10.1175/MWR-D-13-00179.1

Zhang, G., & McFarlane, N. (1995). Sensitivity of climate simulations to the parameterization of cumulus convection in the Canadian Climate Center general-circulation model. *Atmosphere-Ocean*, *33*(3), 407–446. https://doi.org/10.1080/07055900.1995.9649539